

High-Performance High-Power Inductor Design for High-Frequency Applications

By

Mansi Vipul Joisher

B.Tech., National Institute of Technology Karnataka (2020)

Submitted to the Department of Electrical Engineering and Computer Science in Partial Fulfillment of the Requirements for the Degree of

Master of Science

at the

MASSACHUSETTS INSTITUTE OF TECHNOLOGY

JUNE 2023

©2023 Mansi Vipul Joisher . All rights reserved.

The author hereby grants to MIT a nonexclusive, worldwide, irrevocable, royalty-free license to exercise any and all rights under copyright, including to reproduce, preserve, distribute and publicly display copies of the thesis, or release the thesis under an open-access license.

Authored by: Mansi Vipul Joisher
Department of Electrical Engineering and Computer Science
May 19, 2023

Certified by: David J. Perreault
Professor of Electrical Engineering and Computer Science
Thesis Supervisor

Accepted by: Leslie A. Kolodziejski
Professor of Electrical Engineering and Computer Science
Chair, Department Committee on Graduate Students

High-Performance High-Power Inductor Design for High-Frequency Applications

by

Mansi Vipul Joisher

Submitted to the Department of Electrical Engineering and Computer Science
on May 19, 2023, in partial fulfillment of the
requirements for the degree of
Master of Science in Electrical Engineering and Computer Science

Abstract

The performance and size of power electronic circuits are greatly impacted by magnetic components. This is especially true at Radio Frequencies (RF) of many MHz and above. In the High Frequency (HF, 3-30 MHz) range, coreless (or "air-core") inductors with a typical quality factor (Q) of 200-300 are conventionally used and are often the major contributor to the overall system's loss and size. Even when they can achieve high Q, air-core inductors can induce electromagnetic interference (EMI) and eddy current loss in surrounding components, thus limiting system miniaturization. With the recent advancements in high-performance, high-frequency magnetic materials, there is interest in leveraging these magnetic materials at RF and replacing lossy air-core inductors with cored inductors to achieve an improved combination of size and loss. This thesis investigates high-power, high-frequency, high-Q cored inductors. This approach leverages high-frequency high-performance magnetic materials, core geometry, and quasi-distributed gaps to achieve a self-shielded inductor that emits less flux outside its physical volume and can be placed close to other circuit components without inducing EMI or eddy current loss. The performance and self-shielding characteristics of the proposed design procedure are experimentally verified for a 500 nH inductor ($Q = 1150$) designed to operate at 13.56MHz with a peak ac current of up to 80 Amps.

Thesis Supervisor: David J. Perreault

Title: Professor of Electrical Engineering and Computer Science

Acknowledgments

I would like to express my deepest gratitude and appreciation to my advisor, Prof. David Perreault, for being a wonderful teacher and advisor. His support and guidance have been invaluable in the development of this thesis.

I would like to thank our collaborators at MKS Instruments for their invaluable contributions and support throughout this research. I would also like to extend my thanks to Rod Bayliss III, Rachel Yang, and Dr. Mike Ranjram for their prior work, which laid the foundation for this thesis. I am grateful to all my undergraduate mentors and Prof. Alex Hanson for their guidance, which ignited my passion for the field of power electronics and inspired me to continue on this path.

Additionally, I would like to acknowledge my friends in LEES for their support and encouragement throughout this process. I would also like to express my gratitude to my friends at MIT who provided a much-needed respite with coffee breaks during challenging days.

Finally, a huge thanks to my parents, Neeta Joisher and Vipul Joisher, for their unwavering belief in me and their constant support. I am also grateful to my loving sister, Heer Joisher, and Nishkam Prabodh for patiently listening to my writing complaints and ensuring that I ate delicious food during the final weeks of thesis writing.

Lastly, a big shoutout to Siddhant Waghjale for providing much-needed assistance with LaTeX syntax issues and countless hours spent on productive Zoom sessions.

Contents

1	Introduction	17
2	Background and Motivation	21
2.1	Air-Core Inductors	21
2.2	High-Frequency High-Power Cored Inductor	23
2.2.1	Experimental Verification	24
2.3	Motivation for Self-Shielded Cored Inductor	26
3	Proposed Self-Shielded RF Inductor Structure and Design	29
3.1	Geometry Overview	29
3.1.1	Magnetic Circuit Model	30
3.2	Detailed Design Breakdown	31
3.2.1	Center Post and Outer Shell Placement	31
3.2.2	Quasi-Distributed Gap Structure	32
3.2.3	Winding and Window Area	33
3.2.4	Outer Shell, End Caps and Copper Shielding	34
3.3	Loss Modeling	34
3.4	Conclusion	36
3.4.1	Loss Predictions Based on the 2D Model	37
3.4.2	Motivation for a Refined Model	37
4	Modeling and Mitigating 3D effects	41
4.1	Phi-directed Fields	41

4.1.1	Modeling Phi-directed Fields	43
4.1.2	Mitigating Phi-directed Fields	45
4.1.3	Mitigation Strategy Comparison	49
4.2	End-Turns Effect	49
4.2.1	Modeling Lost Gaps	51
4.2.2	End Cap Flux Imbalance	54
4.2.3	Current Crowding	55
4.3	Conclusion	55
4.3.1	Refined Loss Model	56
4.3.2	Results	59
5	An example 500 nH design	61
5.1	Optimizing Inductor Design	61
5.1.1	Design Constraints	62
5.1.2	Optimized Design Details	63
5.2	ANSYS 3D Simulations	64
5.2.1	Winding Return Path Modification to Minimize Loss	66
5.2.2	End-Cap Shrinking to Reduce Size	68
5.3	Equivalent Air-core Simulations for Comparison	69
5.4	Thermal Considerations	71
5.4.1	Thermal Modeling	71
5.4.2	ICEPAK Simulations	72
5.5	Conclusion	73
6	Experimental Verification	75
6.1	Construction	75
6.2	Experimental setup	78
6.2.1	Transformer-based Resonant Tank Setup	79
6.2.2	Challenges	81
6.2.3	Matching Network and Transformer Resonant Tank Setup	82
6.2.4	Measurement Procedure	85

6.3	High-Q Results	87
6.4	Self-Shielding Results	88
6.5	Comparison with an Air-Core Inductor	89
6.5.1	Verification of the Measurement Setup	89
6.5.2	Q-Degradation	91
6.6	Conclusion	91
7	Conclusion	93
7.1	Key Takeaways	93
7.2	Future Work	94
A	Optimization Script : 2D Model	95
B	Optimization Script : 3D Effects Model	99
C	Ferrite core Drawings	117
D	Thermal Model	121
E	Voltage Divider PCB	125

List of Figures

2-1	Flux distribution for an example 709 nH air-core inductor designed in [1]. 4 turns, 9.5 diameter tube, coil inner diameter of 58mm, and coil pitch of 19.53mm.	22
2-2	3D model and 2D polar cutaway model for the proposed inductor in [17]. Design details can be found in Chapter 4 of [17]	24
2-3	Transformer coupled resonant tank experimental setup used in [17] for Q-measurements at high frequency and high current level	25
2-4	Magnetic flux distribution for the proposed inductor in [17]	26
3-1	Schematic Polar Cutaway of proposed Self-Shielded Inductor	30
3-2	3D view of the proposed self-shielded inductor	30
3-3	Self shielded inductor equivalent magnetic circuit	31
3-4	Schematic Polar Cutaway of proposed Self-Shielded Inductor	34
4-1	Net Z-directed current	42
4-2	Phi-directed fields due to the Z-directed current in the design shown in Table 3.1	42
4-3	A single outer shell core piece	43
4-4	Magnetic circuit model for a single outer shell core piece	43
4-5	Stack of outer shell core pieces	45
4-6	Magnetic circuit model for a single outer shell core piece accounting for the fringing field through the shell gap	45
4-7	Inductor inductance and performance vs notch angle	47

4-8	Helical winding with a return path through the notch : minimizes z-directed current	48
4-9	Winding split into two halves with z-directed currents in opposite direction: minimizes z-directed current	48
4-10	Double layer winding : eliminates z-directed current	48
4-11	Impact of mitigation strategies on the phi-directed fields for 500 nH self-shielded inductor designs (A) Inductor design details in Table 3.1 (B) Design in A with outer shell modification total notch angle = $\frac{\pi}{3}$ (C) Design in A with a winding return path (z-distance between input and output terminals = 10 mm)	50
4-12	H-field distribution on the YZ Cross-Section of a self-shielded Inductor, design details in Table. 3.1, highlighting the tendency of fields to bridge the winding gap near the window ends. (a) Unobstructed view highlighting 'lost gaps' with arrows. (b) Core shell locations included for reference.	51
4-13	Window gap reluctance estimation	52
4-14	Modified magnetic circuit model for z-directed fields that accounts for the additional reluctance due to lost gaps	53
4-15	B-field distribution on the YZ Cross-Section of a self-shielded Inductor, highlighting the field imbalance in endcaps and radial dependency due to Phi-directed fields. Lost gaps marked with arrows.	54
4-16	Core loss distribution in the top and bottom endcap confirming that flux imbalance in end caps due to end turns effect	54
4-17	Front view and top view of the proposed inductor design with geometrical parameters	56
5-1	Side view of the optimized self-shielded inductor design. End-caps shrunk based on 5.2.2	63
5-2	B-field distribution in outer shell and center post for the optimized inductor design. Below 20 mT to avoid whapping.	65

5-3	Loss distribution in the optimized inductor. Total loss = 85 W. . . .	66
5-4	Self-shielded cored inductor simulation with a return path for winding. Design details in Table 5.3. The distance between the return path and the winding was optimized through sweep in simulations. Z-displacement between input and output terminal = 20 mm, radial distance between return path and winding = 7 mm	67
5-5	Loss analysis comparison for optimized design with and without return winding path	67
5-6	B-field distribution in end-caps suggest they are oversized	68
5-7	Thermal Model in terms of part modules	71
5-8	ICEPAK simulation of center post, outer shell and end caps @ Tambient = 22 deg Celcius	72
5-9	ICEPAK simulation of center post, outer shell and end caps @ Tambient = 100 deg Celcius	73
6-1	Polypropylene non-magnetic spacers cut using a waterjet cutter . . .	76
6-2	Center post and one fourth of the outer shell stacked using core pieces and spacer material, number of gaps = 13	76
6-3	PTFE hollow cylinder machined to achieve desired height, outer and inner diameter	77
6-4	Cooper foil wrapped around center post through the PTFE support structure using double-sided polyimide tape	77
6-5	3D printed ULTEM structure to house outer shell and support shield	78
6-6	Top view of the center post, outer shell and copper winding	78
6-7	End caps enclosure the center post, winding and outer shell axially .	79
6-8	75 μ m thick copper foil is wrapped around the structure to eliminate any fringing fields	79
6-9	Transformer coupled resonant tank experimental setup used in [3],[17] for Q-measurements at high frequency and high current level	80

6-10	Matching network and transformer coupled resonant tank experimental setup for Q-measurements at high frequency and high current level	82
6-11	Capacitive voltage divider consisting of ten 2.2 pF capacitors in series with a 22 pF capacitor used to measure the resonant voltage across the vacuum capacitor. PCB layout shown Appendix E.	83
6-12	Calibration of the voltage divider ratio to estimate the total voltage across the vacuum capacitor	85
6-13	An annotated photo of the test setup	86
6-14	Experimental Q-Measurements for the proposed design	87
6-15	Q-masurments of the proposed inductor in close proximity (25 mm) to a vacuum capacitor	88
6-16	Q-measurments to highlight the self-shielded characteristics of the design	89
6-17	Air-core inductor series resonant network with a vacuum capacitor. Air-core specifications : 3 turns of 16 mm copper (wall thickness of 1 mm). Inner radius of the solenoid = 40 mm, pitch = 32 mm.	90
C-1	Drawing of Ferrite Center Post Piece	118
C-2	Drawing of Ferrite outer shell Piece	119
C-3	Drawing of Ferrite End Cap	120
D-1	Thermal resistance 'modules' used to define thermal resistance network	121
D-2	First set of thermal resistances used in the thermal model.	122
D-3	Second set of thermal resistances used in the thermal model.	123

List of Tables

3.1	Geometry of the optimized self-shielded inductor based on the 2D loss model	37
3.2	Comparison Between 2D and 3D ANSYS simulations and 2D Model based MATLAB Predictions of Self-Shielded Inductor Structure [17] * Simulation doesn't include winding skin effect	38
4.1	Predicted phi-directed field using reluctance models vs the phi-directed field seen in 3D ANSYS simulations	44
4.2	Comparison between the refined model-based prediction and 3D ANSYS simulations of the Self-Shielded Inductor Structure	59
5.1	Geometry of the optimized self-shielded inductor.	64
5.2	Simulated losses in the optimized 500nH self-shielded inductor	64
5.3	Updated Geometry of the optimized self-shielded inductor post end cap shrinking	69
5.4	Optimized self-shielded cored inductor compared to equivalent loss and volume shielded air-core inductors	70

Chapter 1

Introduction

Power converters operating in the high-frequency (HF, 3- 30MHz) band of the Radio-Frequency (RF) spectrum offer numerous potential advantages such as better performance, reduced energy storage requirements, and miniaturization [16]. Moreover, certain applications (e.g., RF plasma generation, HF wireless power transfer) naturally require a high-frequency operation due to the nature of the system, To reap maximum benefits from operating in the HF regime, all the individual components should operate efficiently at these frequencies. However, the design of efficient power magnetic components for operation at HF and above is particularly a challenging task. In conventional power converter designs at lower frequencies, magnetic components are often equipped with a core to enable miniaturization, high efficiency, and self-shielding as the core material assists in concentrating the magnetic field and reduces losses. However, as the operating frequency increases, both copper and core losses become significant obstacles, posing a considerable challenge for the design of cored magnetics in HF applications.

The increase in frequency affects the behavior of magnetic materials, including commonly used core materials like MnZn ferrites, which tend to exhibit poor performance with high core losses above a few MHz [21]. Additionally, the skin effect and proximity effect make it challenging to effectively carry large currents at HF frequencies. Techniques such as using Litz wire to compensate for these losses become impractical at frequencies beyond a few MHz due to manufacturing constraints

[21]. Consequently, air-core (coreless) inductors are prevalent in RF applications, and dominate the HF (3-30 MHz) and VHF (30-300 MHz) frequency ranges (e.g., [25],[1]).

While air-core RF inductors provide advantages such as simplicity and ease of fabrication, they suffer from a significant drawback. The absence of a core means that the magnetic field generated by the inductor is not shielded and can couple with other components in the system. This often results in electromagnetic interference (EMI) and induces significant losses due to eddy currents. As a result, RF air-core inductors often require a significant physical volume and may need to be placed in a metal enclosure, isolated from the control circuitry, to mitigate EMI and preserve high efficiency [1][18]. Consequently, air-core RF inductors can be a major bottleneck for system miniaturization and overall efficiency, affecting applications like tunable matching networks [1].

The strong desire to achieve higher efficiencies and power densities for RF applications has led to tremendous progress in the measurement and characterization of high-performance magnetic material at HF [7],[9]. It has been found that low-permeability NiZn ferrite materials are particularly suitable for high-frequency ac inductor design. Proper design of cored inductors leveraging these materials can provide better combinations of size and efficiency than coreless inductors [8],[23],[24],[3],[19]. Achieving high-performance cored HF inductors also necessitates employing design techniques to mitigate the adverse effects of skin and proximity losses. Techniques such as field balancing to reduce skin effect loss and quasi-distributed gaps [10] to minimize proximity effect losses have shown potential in mitigating these challenges for applications up to 3 MHz [23],[24]. Recent work presented in [3] using these new design techniques and low-permeability RF magnetic materials has achieved impressive efficiency for high-power RF applications at 13.56 MHz.

However, many of these designs result in significant magnetic fields surrounding the inductor, with attendant EMI concerns. These losses become even more pronounced at higher frequencies and cannot be ignored. For instance, the high-power cored inductor described in [3] achieves impressive efficiency by minimizing losses, but it still generates substantial external fringing flux, much like its air-core solenoid

counterpart. The unshielded nature of this inductor's external field can result in unwanted coupling with surrounding components, leading to induced losses and EMI. Consequently, there is a clear demand for cored HF inductors that not only deliver high efficiency but also provide effective self-shielding to minimize induced losses and EMI in the surrounding components.

This thesis builds upon the RF-cored inductor design presented in [3], [17] and presents a high-quality factor (Q)¹ 'self-shielded' inductor. The proposed inductor is specifically designed to minimize the generation of magnetic fields outside its physical volume and hence, called 'self-shielded'. By incorporating self-shielding techniques, the inductor aims to mitigate electromagnetic interference concerns and induced eddy current losses. This is accomplished while maintaining many of the efficiency and performance benefits of the HF designs in [23],[24],[3].

Chapter 2 provides background regarding the disadvantages associated with the use of conventional air-core inductors for high-power RF applications. It also provides a comprehensive review of prior research, as presented in [17], focusing on the design of high-frequency, high-power cored inductor. This previous work serves as a fundamental reference for the proposed design that will be introduced subsequently. Additionally, the chapter presents the motivation behind the need for the proposed design.

Chapter 3 presents a novel inductor structure specifically designed for high-power RF applications, emphasizing low-loss characteristics. The design accomplishes an optimized combination of size and performance by incorporating field balancing, and quasi-distributed gaps to minimize loss along with self-shielding techniques to constrain its effective size. The chapter also provides a 2D model to predict loss in the inductor. Additionally, the chapter presents the motivation behind the need for advancements and modifications to the 2D model.

In Chapter 4, a critical evaluation is conducted to assess the disparity between the predictions obtained from the 2D model and the ANSYS simulations. The observed

¹Inductor quality factor (Q) in this document is defined as $Q = \frac{\omega L}{R_L}$, where R_L is the equivalent series resistance of the inductor at the frequency of interest [6]

discrepancies can be attributed to the influence of 3D effects resulting from the low-turn winding configuration. To address this limitation, a novel model is developed, taking into account the intricate 3D effects, thereby enabling accurate prediction of the total loss in the inductor. Furthermore, various geometrical strategies are explored to mitigate the impact of the 3D effects observed in the inductor design. A refined model is presented to predict the loss in the proposed inductor.

Chapter 5 utilizes the refined and improved model developed in Chapter 4. Building upon the design guidelines established in Chapter 3, this chapter presents an optimized low-loss self-shielded inductor with a nominal value of 500 nH operating at a frequency of 13.56 MHz, with a peak ac current of 80 A. Simulation results are provided to verify the high-Q (simulated to be approximately 1450) of the proposed design. The thermal viability of the design is also analyzed.

Chapter 6 focuses on providing construction guidelines for the simulated 500 nH inductor example. In order to validate the design and its performance, an experimental setup is proposed. The Q of the designed inductor is measured and confirmed to be approximately 1150 at the full drive level. The self-shielding characteristics of the inductor design are also thoroughly verified. The design is compared to a conventional air-core inductor to highlight the distinct advantages offered by the proposed design over the traditional air-core counterpart.

Chapter 7 summarizes key takeaways from this thesis and discusses future work.

Chapter 2

Background and Motivation

In this chapter, we will discuss the limitations and drawbacks of conventionally used air-core inductors for high-power Radio Frequency (RF) applications. We will also provide an overview of previous research presented in [3][17] on high-frequency high-power cored inductor design that serves as the foundation and basis for the proposed design. Furthermore, we will present the motivation behind the development of the proposed high-performance high-power high-frequency self-shielded cored inductor design.

2.1 Air-Core Inductors

Air-core inductors (solenoids) are conventionally used for RF power applications. However, they often dominate the system's size and contribute significantly to the overall losses. One significant drawback is the uncontrolled nature of the H-field and B-field intensity distribution within and around the inductor. As depicted in figure 2-1, the H-field intensity is highest at the center of the coil and quickly diminishes towards the outer regions. This imbalance in the magnetic field results in a skin depth effect, where current is concentrated on the side with higher magnetic field density, leading to significantly increased winding loss due to unused conduction area at high frequencies. Additionally, the fringing magnetic field generated by air-core inductors can induce eddy currents in nearby metal structures. These eddy currents cause

electromagnetic interference (EMI) losses and can adversely affect the performance of neighboring components or circuits. To mitigate these EMI losses, one often places such air-core inductors within a metal enclosure [18](e.g, [1]). However, placing a metal enclosure around an air-core inductor affects the inductance and the overall performance of the system.

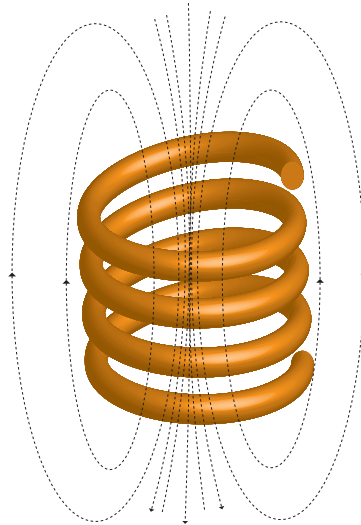


Figure 2-1: Flux distribution for an example 709 nH air-core inductor designed in [1]. 4 turns, 9.5 diameter tube, coil inner diameter of 58mm, and coil pitch of 19.53mm.

For example, to estimate the effective volume of the example 500 nH air-core inductor operating at 13.56 MHz with a peak ac current of up to 80 Amps (as shown in the figure 2-1), we consider the minimum volume of a hollow copper cylinder that can be placed around the inductor without causing degradation of its quality factor or inductance by more than 5%. The estimated effective volume for this particular air-core inductor is approximately 39L (the hollow cylindrical shield is 180 mm tall and the inner radius is 270 mm). Instead, if we instead we place a smaller shield volume of 4.5 L (100 mm tall and inner radius of 120 mm) which is almost 5 times the physical volume of the inductor, we estimate that the inductance degrades by almost 25% in this case. This observation highlights that a large volume area is needed around an air-core solenoid to prevent performance degradation. The significant inductance and quality factor degradation effect indicates the importance of carefully considering the design and placement of the enclosure to minimize its impact on the inductor's

performance.

Air-core inductors have drawbacks such as high losses and large physical size as mentioned above, which makes the transition to cored inductors for RF applications appealing. However, this transition has been challenging primarily due to the limitations of traditional high-permeability magnetic materials as these are not suitable for efficient RF inductor designs. These materials exhibit poor performance including high losses, hindering the development of effective cored inductors.

Nevertheless, recent advancements in the measurement and characterization of magnetic core materials have focused on addressing these limitations, particularly for RF applications operating in the tens of MHz range [7],[9]. These advancements have sparked research and exploration into the design and development of magnetic core inductors as an alternative to conventionally used air-core inductors. The following subsections briefly discuss two high-frequency high-power cored inductor designs presented in [17].

2.2 High-Frequency High-Power Cored Inductor

A high-frequency high-power RF cored inductor design leveraging high performance magnetic material and core geometry is proposed in [3][17]. The design aims to achieve improved performance compared to an air-core inductor for operating frequencies near 13.56 MHz. The inductor structure as shown in figure 2-2 features a dumbbell-shaped core geometry consisting of two end caps and a center post. The winding is wound around the center post. The center post is a quasi-distributed gap structure constructed using alternating discs of magnetic core material and non-magnetic spacer material, allowing control over the reluctance of the center post. The end caps of the inductor shape the flux path, helping to minimize the portion of the flux that fringes axially out of the core.

The design approach incorporates several key elements to achieve an improved performance magnetic-core inductor. Firstly, it utilizes a high-performing low-permeability magnetic materials (Fair-rite 67) to enhance the inductor's efficiency. Additionally,

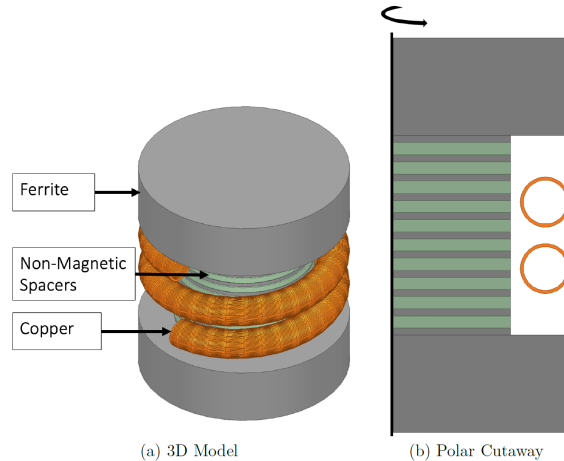


Figure 2-2: 3D model and 2D polar cutaway model for the proposed inductor in [17]. Design details can be found in Chapter 4 of [17]

quasi-distributed gaps are employed in the center post of the inductor to address winding and core losses at RF. This arrangement effectively reduces eddy current losses caused by the magnetic fields fringing from one large gap. The design strategy focuses on achieving balanced magnetic field strength on multiple sides of the winding in order to increase the effective conduction area. This balancing of magnetic fields helps to mitigate the higher conduction losses that occur due to skin effect at higher frequencies. Through field balancing, the design achieves double-sided conduction in the winding and thereby reducing winding losses, and improving efficiency compared to the traditional single-sided conduction approach.

2.2.1 Experimental Verification

A 500 nH example inductor was presented operating at 13.56 MHz up to an ac peak current of 80 Amps. The structure used Fair-rite's 67 ($\mu_r = 40$) material as its core material due to its exceptional performance factor at the frequency of interest. The performance of the inductor was measured by measuring the Q of the inductor. A variant of the resonant tank method described in [7] was used for Q-measurements. The measurement setup as shown in figure 2-3 was used. The cored inductor is resonated with a low-loss vacuum capacitor and transformer coupled to an RF power amplifier to drive pure-tone, high-current sinusoids into the system. The measurement

setup details can be found in [17]. Through the resonant tank measurement technique, the quality factor (Q) and resistance of the inductor (R_L) can be estimated using the equations shown below. R_c is the equivalent series resistance (ESR)¹ of the vacuum capacitor and R_x is the additional resistance due to connection leads in the LC tank.

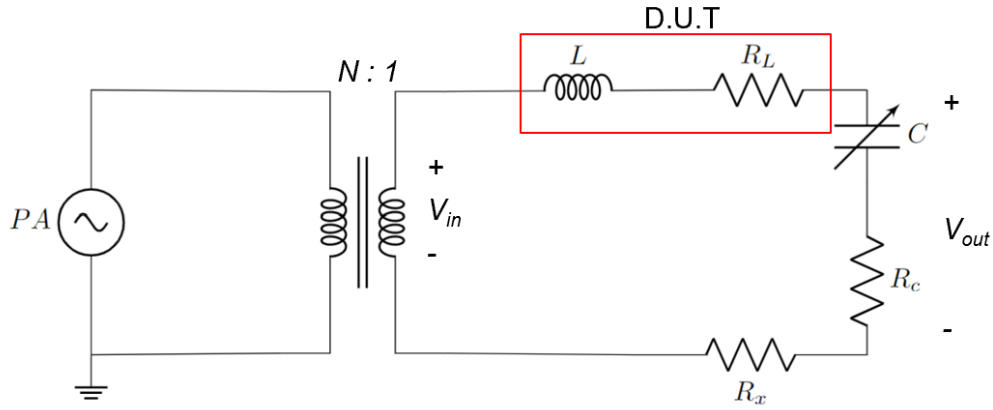


Figure 2-3: Transformer coupled resonant tank experimental setup used in [17] for Q-measurements at high frequency and high current level

$$\frac{V_{out}}{V_{input}} = \frac{1}{1 - \omega^2 CL + (j\omega C)(R_L + R_c + R_x)} \quad (2.1)$$

At resonance:

$$\frac{v_{out}}{v_{in}} = \frac{1}{\omega C(R_L + R_c + R_x)} \quad (2.2)$$

$$R_L = \omega L \cdot \frac{V_{in,pk}}{V_{out,pk}} - R_x - R_c \quad (2.3)$$

The 500 nH design was estimated to have a Q of approximately 1100 up to $20A_{pk}$ current at 13.56 MHz (more than 2 times of an equivalent air-core inductor). The high-frequency high-power cored inductor design discussed above has shown significant improvements in reducing loss and achieving a higher quality factor compared to air-core inductors.

¹The ESR for the vacuum capacitor can be found from their datasheet and R_x can be estimated through FEA simulations

2.3 Motivation for Self-Shielded Cored Inductor

One limitation of the inductor design discussed above is the distribution of magnetic flux outside its physical volume. The magnetic flux flows far away from the inductor as shown in figure 2-4. While coreless (air-core) inductors suffer from the same issue as discussed in section 2.1, reducing the flux outside of the core can offer significant performance improvements.

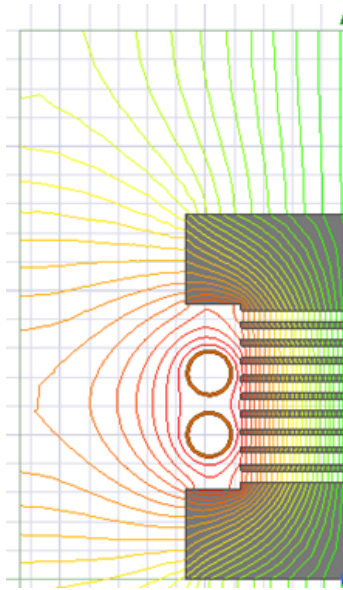


Figure 2-4: Magnetic flux distribution for the proposed inductor in [17]

In the field of RF plasma generation, there is a strong desire to decrease the size of enclosures that house the RF power electronics, while also ensuring that all power electronics are contained within a metal enclosure to reduce electromagnetic interference and loss in surrounding components. One motivation for this is to enable smaller power amplifiers and matching networks that can be mounted close to or on the plasma chamber. There is also a desire for the higher efficiencies needed to miniaturize the enclosure.

However, placing a metal object perpendicularly to a time-varying magnetic field generates eddy currents and loss, reducing system efficiency and practically decreasing inductance. This presents a significant problem for coreless inductors and the cored inductor design discussed above, as the surrounding boxes must be physically large

to prevent losses. Magnetic materials are a key means to prevent the magnetic fields from inducing loss in the box.

Hence, To overcome this limitation, an initial design framework for a self-shielded cored inductor is proposed in chapter 6 of [17]. As the name suggests, the self-shielded inductor is designed in a way to make sure there is no magnetic flux outside of its physical volume. The original dumbbell-shaped structure discussed above has been transformed into a pot core structure by incorporating an outer core. This addition serves as a return path for the flux that may otherwise leak out and enables a degree of field balancing. Furthermore, a conductive shield is wrapped around the inductor to eliminate fringing H-fields. By reducing the size and volume of the inductor, various simultaneous benefits can be achieved, such as increased efficiency, improved space utilization, and enhanced overall system performance.

Chapter 3

Proposed Self-Shielded RF Inductor Structure and Design

This chapter introduces the design of a self-shielded inductor for high-current (tens of amps) and radio frequency (10s of MHz) applications. The work here upon and substantially expands on that presented in [17][17]. The proposed structure is designed to achieve a low-loss cored inductor while effectively containing the magnetic flux within its physical volume, hence the name 'self-shielded'. Additionally, a 2D analysis-based total loss function for the inductor is derived in terms of other design variables as the goal is to optimize the design for minimum total loss for a given inductance and volume. The chapter also analyzes the accuracy of this model and discusses the need for a refined or improved model.

3.1 Geometry Overview

The proposed inductor design comprises a specialized pot-core structure with an outer shield as illustrated in Fig. 3-1. It includes a center post, an outer shell, two end caps, a single-layer winding, and a copper shield. The center post is constructed using magnetic and non-magnetic discs in an alternating pattern to create a quasi-distributed gap structure. The outer shell also consists of alternating magnetic and non-magnetic rings and serves as a path for the flux return within the physical volume

of the inductor. The outer shell rings has one or more notches to facilitate the entry and exit of the winding to the window area. The single-layer winding has evenly spaced turns and is wound around the center post. The winding uses one of the outer shell rings notches to enter and exit the window area. The end caps enclose the winding and are used to shape the flux path, reducing the axial fringing of the flux. The entire structure is wrapped in a copper shield, which rejects leakage flux flowing out of the structure.

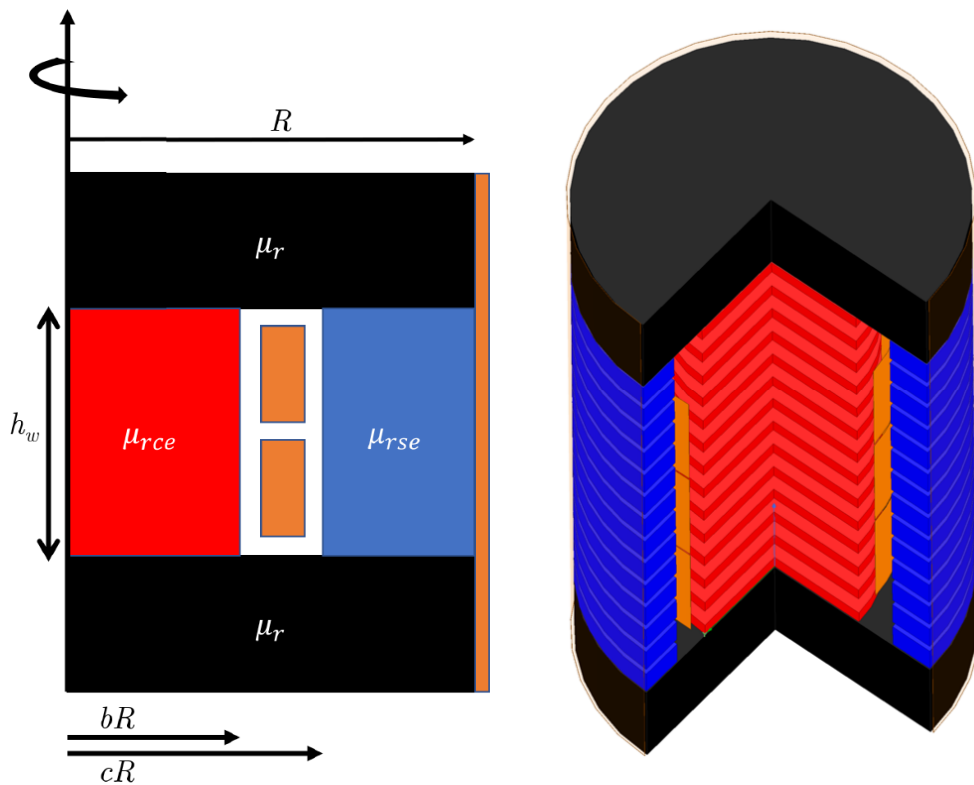


Figure 3-1: Schematic Polar Cutaway of proposed Self-Shielded Inductor

Figure 3-2: 3D view of the proposed self-shielded inductor

3.1.1 Magnetic Circuit Model

The magnetic circuit model for the proposed self-shielded inductor is as shown in Fig. 3-3. \mathcal{R}_{center} , \mathcal{R}_{shell} , and \mathcal{R}_{endcap} are the reluctances corresponding to the center post, outer shell, and end caps. N is the number of turns on the winding and I is the

current in the winding. The copper shield wrapped around the inductor is shorted to eliminate fringing H-fields, and its influence on the inductance and loss is considered in the magnetic circuit model and design. The lossy nature of the shield is modeled as a transference element \mathcal{L}_{shield} [15][11]. The net reluctance of the structure is \mathcal{R}_{net} and the inductance of the proposed inductor L_{net} can be expressed as :

$$\mathcal{R}_{net} = \mathcal{R}_{center} + \mathcal{R}_{shell} + 2\mathcal{R}_{end\ cap} \quad (3.1)$$

$$L_{net} = \frac{N^2}{\mathcal{R}_{net}} \quad (3.2)$$

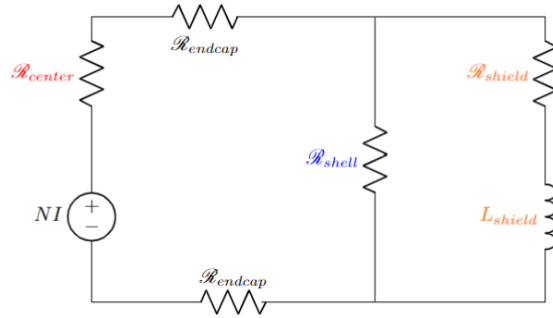


Figure 3-3: Self shielded inductor equivalent magnetic circuit

3.2 Detailed Design Breakdown

In this subsection, we discuss how the proposed self-shielded inductor is designed to achieve a superior combination of size and Q (quality factor) compared to a conventional air-core inductor. The key focus is on how the design optimizes the geometry of the center post and outer shell, as well as the winding and copper shield, to minimize the total loss in the inductor and the flux outside its physical volume.

3.2.1 Center Post and Outer Shell Placement

In an air-core solenoid, as depicted in Fig. 2-1, the H-field intensity is not uniformly distributed along the coil. The intensity of the H-field is the highest at the center

of the coil and gradually decreases towards the outer edges. When the solenoid is operated at high frequencies, the current carrying capability of the conductor is limited due to the skin effect. This effect causes the current to be concentrated on the surfaces of the conductor that experience the largest magnetic fields. Consequently, only a fraction of the total conductor cross-section is effectively utilized for current conduction. This results in an increase in copper loss due to the reduced conduction area.

The placement of the center post and outer shell in the proposed self-shielded inductor makes it possible to regulate the distribution of H-fields throughout the inductor. This improved distribution of H-fields allows for a larger portion of the winding area to be utilized for current conduction. In an unshielded design, the optimal center-post magnetomotive force (MMF) percentage is 50% i.e. fields are balanced on the sides of the winding [23][24], as described in section 2.2. This type of conduction results in a significant reduction of copper loss, down to as little as half the single-sided conduction case. However, with the introduction of the shield, the optimal balance shifts towards a higher center-post MMF percentage of approximately thrice the outer core flux as higher center-post MMF results in lower loss in the outer shell core and shield.

3.2.2 Quasi-Distributed Gap Structure

An optimal cored magnetic design balances core and winding loss, and stores a large fraction of the total energy in the gaps of the structure [12]. In the realm of high-frequency and high-current applications, this tends to require large gaps (or low equivalent permeability). However, using discrete gaps yields large fringing fields and consequent proximity effect losses. These fringing fields from the gap can induce unwanted currents in the nearby winding, causing additional losses. So, the proposed structure incorporates a quasi-distributed gap structure [10][23][24] for the center post and the outer shell. Instead of utilizing a single large gap, multiple smaller gaps are strategically distributed along the core. The quasi-distributed gap structure allows for a more even distribution of the MMF across the gaps. This prevents the entire

MMF from being concentrated in a single gap, which can result in higher losses. By dividing the MMF among multiple gaps, the total loss in the winding is reduced, leading to improved overall efficiency. The selection of the pitch-to-spacing ratio between the gaps and conductors as recommended in [10] ($p < 4s$) is observed to minimize fringing losses.

The calculation of μ_{rec} and μ_{res} , the relative effective permeability of the center-post and outer-shell, is done using the given effective ferrite permeability μ_{rf} and the ferrite fraction f_f , which represents the fraction of ferrite relative to the total of the ferrite and gap lengths.

$$f_f = \frac{l_{ferrite}}{l_{ferrite} + l_{gap}} \quad (3.3)$$

$$\mu_{rec} = \frac{\mu_{rf}}{f_{f,c} + \mu_{rf}(1 - f_{f,c})} \quad (3.4)$$

3.2.3 Winding and Window Area

The Fig. 3-1 illustrates a 2D polar view of the proposed inductor. The winding is wound around the center post and is surrounded by the outer shell. The area between the center post and the outer shell that encloses the winding is called the window area. A notch is provided in the outer shell that serves as an entry and exit point for the winding. The top view of the center post, winding and outer shell is as shown in Fig. 3-4. To minimize copper loss and optimize the utilization of the window area, the proposed inductor employs a single-layer of copper foil as the winding structure.

At frequencies in the range of a few MHz, the skin depth of copper is typically in the range of micrometers. Therefore, using a copper foil that is 50 μm thick provides more than enough conduction area for efficient current flow. This approach ensures that a significant portion of the conductor's cross-sectional area is effectively utilized, minimizing conduction loss associated with unused conductor area. By opting for a single-layer winding, the proposed inductor design minimizes the proximity effect. Furthermore, by utilizing a single-layer copper foil, the proposed inductor can achieve a compact and space-efficient design.

3.2.4 Outer Shell, End Caps and Copper Shielding

The outer shell plays a crucial role in the self-shielded inductor design. It acts as a pathway for the magnetic flux generated by the current flowing through the winding to return within the physical envelope of the inductor while enabling a controlled field distribution along the winding. By confining the flux within the inductor, minimizes magnetic flux leakage to the surrounding environment, reducing inductance and loss sensitivity to nearby objects.

To prevent axial flux leakage from the inductor, two end caps are utilized, enclosing the winding at both ends. Additionally, a copper shield is wrapped around the structure to further enhance magnetic field containment and minimize external fringing effects.

3.3 Loss Modeling

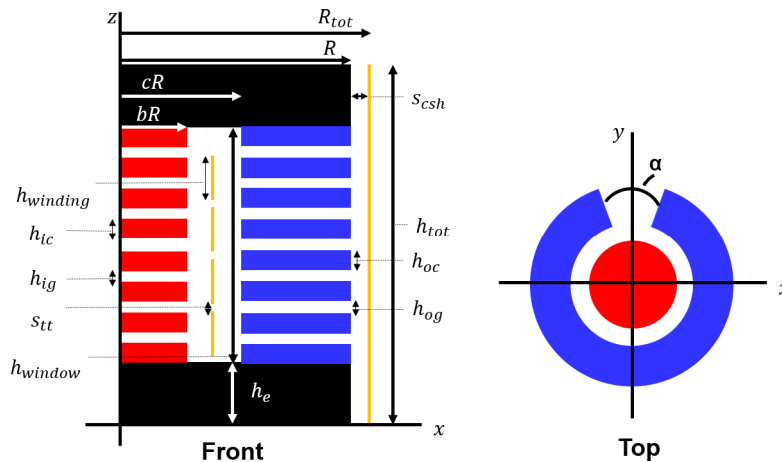


Figure 3-4: Schematic Polar Cutaway of proposed Self-Shielded Inductor

Our goal is to achieve an optimal design for a given inductance and volume by considering all the parameters shown in Fig. 3-4. Having a model function is essential for optimization purposes so we start by modeling the loss in our self-shielded inductor. The total loss in the inductor is the sum of the copper (winding) loss and core loss. The loss in the copper windings and shield is determined by considering the

MMF on both sides of the winding. It is assumed that the shield effectively rejects all flux, and We assume that there is a skin depth (δ) of conduction on either side of the winding (copper foil).

$$\text{LOSS} = P_{\text{core,center}} + P_{\text{core,shell}} + P_{\text{core,end caps}} + P_{\text{winding,inner}} + P_{\text{winding,outer}} + P_{\text{shield}} \quad (3.5)$$

Reluctances of center post, outer shell and end caps are defined as :

$$\mathcal{R}_{\text{center}} = \frac{h_w}{\mu_{\text{rec}}\mu_0\pi b^2 R^2} \quad (3.6)$$

$$\mathcal{R}_{\text{shell}} = \frac{h_w}{\mu_{\text{res}}\mu_0\pi R^2(1 - c^2)} \quad (3.7)$$

$$\mathcal{R}_{\text{end cap}} = \frac{(1 + c)}{\mu_r\mu_0\pi 2h_e} \quad (3.8)$$

Where, μ_{rec} and μ_{res} can be found from equation 3.4 and μ_r is the relative permeability of the core material. The MMF drop across $\mathcal{R}_{\text{center}}$ is $\mathcal{F}_{\text{inner}}$ and MMF across $\mathcal{R}_{\text{shell}}$ is $\mathcal{F}_{\text{outer}}$.

$$\mathcal{F}_{\text{inner}} = \frac{\mathcal{R}_{\text{center}}}{\mathcal{R}_{\text{center}} + \mathcal{R}_{\text{shell}} + 2\mathcal{R}_{\text{end cap}}} NI \quad (3.9)$$

$$\mathcal{F}_{\text{outer}} = \frac{\mathcal{R}_{\text{shell}}}{\mathcal{R}_{\text{center}} + \mathcal{R}_{\text{shell}} + 2\mathcal{R}_{\text{end cap}}} NI \quad (3.10)$$

$$P_{\text{winding,inner}} = \frac{1}{2} \left(\frac{\rho_{\text{cu}}}{h_{\text{winding}}} \frac{2\pi b R}{\delta} \right) \mathcal{F}_{\text{inner}}^2 \quad (3.11)$$

$$P_{\text{winding,outer}} = \frac{1}{2} \left(\frac{\rho_{\text{cu}}}{h_{\text{winding}}} \frac{2\pi c R}{\delta} \right) \mathcal{F}_{\text{outer}}^2 \quad (3.12)$$

$$P_{\text{shield}} = \frac{1}{2} \left(\frac{\rho_{\text{cu}}}{h_{\text{tot}}} \frac{2\pi R_{\text{tot}}}{\delta} \right) \mathcal{F}_{\text{outer}}^2 \quad (3.13)$$

The magnetic field density is evaluated in the core pieces to estimate the core loss using the Steinmetz equation [20]. I is the peak of the ac current through the inductor. L is the net inductance and can be calculated using equations 3.1 and 3.2.

$$B_{\text{center}} = \frac{LI}{N\pi b^2 R^2} \quad (3.14)$$

$$B_{\text{shell}} = \frac{LI}{N\pi(1 - c^2)R^2} \quad (3.15)$$

$$B_{\text{end cap}} = \frac{LI}{N\pi R h_e} \quad (3.16)$$

The expressions for calculating the core losses in the center post, outer shell, and end cap of the inductor are as follows:

$$P_{\text{core,center}} = f_{f,c} C_m f^\alpha B_{\text{center}}^\beta \pi b^2 R^2 h_w \quad (3.17)$$

$$P_{\text{core,shell}} = f_{f,s} C_m f^\alpha B_{\text{shell}}^\beta \pi (1 - c^2) R^2 h_w \quad (3.18)$$

$$P_{\text{core,end caps}} = 2C_m f^\alpha B_{\text{shell}}^\beta \pi R^2 h_e \quad (3.19)$$

C_m , α and β are Steinmetz parameters for the core material and can be extracted from the datasheet for a frequency of interest.

3.4 Conclusion

A MATLAB script was developed based on the 2D analysis presented above to optimize the total loss in the inductor for a given inductance and volume (Appendix A). The inductance was set to 13.56 MHz, with an inductance $L = 500$ nH and the volume of the inductor was constrained to 1L. The inductor was designed to operate at 500 nH and a peak ac current of 80 A. The design details are provided in Table 3.1.

Volume	1L
Inductance	500 nH
End-cap radius	43 mm
Center-post radius	23.65 mm
Outer-shell inner radius	26.74 mm
Winding radius	33.24 mm
End-cap height	36 mm
Number of gaps	20
Number of turns	4
Center-post core piece height	3.27 mm
Outer-shell core piece height	4.84 mm
Winding foil height	23.79 mm
Winding turn-to-turn spacing	1 mm
Winding foil thickness	51 μ m
Core material	Fair-rite 67

Table 3.1: Geometry of the optimized self-shielded inductor based on the 2D loss model

3.4.1 Loss Predictions Based on the 2D Model

The loss predicted from the 2D model based MATLAB script is compared to 2-D and 3-D ANSYS finite element analysis (FEA) simulations as shown in Table 3.2. The findings show reasonable agreement between the 2D Model and 2D simulation, with the MATLAB script slightly underestimating inductance and loss in a proportional manner to match the estimated quality factor. The results demonstrate a significant reduction in loss compared to an air-core inductor ($Q = 600$). Additionally, this design allows for a much smaller volume requirement as the magnetic fields are confined within its physical boundaries.

3.4.2 Motivation for a Refined Model

The results presented in Table 3.2 indicate that the 2-D model and 2-D ANSYS simulation provide relatively accurate estimations of inductance, copper loss, core

	2-D Model	2-D ANSYS	3-D ANSYS
Inductance (nH)	500	623.45	790
Copper Loss (W)	56.21	63.81	82*
Core Loss (W)	32.57	46.31	191
Total Loss (W)	88.69	110.1	>273
Quality factor'	1535	1544	< 788

Table 3.2: Comparison Between 2D and 3D ANSYS simulations and 2D Model based MATLAB Predictions of Self-Shielded Inductor Structure [17]

* Simulation doesn't include winding skin effect

loss, total loss, and quality factor. However, when we compared them to the 3-D ANSYS simulation, both the 2-D model and 2-D ANSYS simulation appear to underestimate the loss and inductance values by approximately 50%. These significant discrepancies highlight the limitations of the 2-D models in accurately capturing the three-dimensional effects present in the self-shielded inductor design. This is mainly due to the fact that these designs often involve very low turn counts, such as 2 or 3 turns, to minimize copper loss. The helical nature of the winding at such low turn counts significantly disrupts the 2-D symmetry, to the extent that infeasible designs can arise if 3-D effects are not considered.

In addition to addressing the 3D effects, it is crucial to address the impact of capacitance on the design of the self-shielded high-power RF cored inductor to maintain a reasonable self-resonance frequency (SRF). Specifically, when considering the core material used, such as Fair-rite 67 with a permittivity range of 12-15 [5]. Even a slight alteration in the core's geometry can have a significant effect on the capacitance and subsequently the SRF. This means that careful consideration must be given to the design to ensure that the desired capacitance and SRF are achieved, as any deviation may render a particular design impractical or unfeasible.

Additionally, thermal considerations also play a critical role in the design and performance of the self-shielded high-power RF cored inductor. The primary objective of this work is not solely focused on achieving a specific loss value or minimizing loss; rather it is primarily centered around reducing the effective volume of the inductor by minimizing magnetic fields outside its physical volume. However, in the

pursuit of reducing the effective volume, it becomes crucial to address the associated thermal constraints. Excessive heat generation can lead to undesirable consequences, including thermal runaway, reduced performance, and even potential damage to the inductor core and surrounding components. Therefore, the question of acceptable loss is intimately linked with the thermal considerations imposed on the design.

Hence, chapter 4 investigates the three-dimensional effects inherent in the design and subsequently modify the design to minimize the total loss. Recognizing the significance of having a reliable model for the loss, It also focuses on developing a three-dimensional-based model for this design. The subsequent chapters also delve into the discussion of capacitance estimation for the inductor and thermal modeling, which aims to evaluate the thermal viability of the design.

By incorporating the insights gained from studying the 3-D effects, and constraining the design to be thermally viable a refined and more accurate loss is developed and, a low-loss optimized self-shielded inductor is designed.

Chapter 4

Modeling and Mitigating 3D effects

As mentioned in Section 3.4.2, it has been determined that a 2D model is not sufficient for accurately predicting the total loss in low-turn inductors. This is due to the fact that the 2D approximation of the turns does not account for the additional losses resulting from the 3D effects of the winding. Therefore, it is necessary to update the 2D-based loss model presented in Section 3.3 to incorporate these 3D effects and obtain a more accurate model for optimization purposes. This chapter focuses on modeling these effects to achieve precise predictions and explores various mitigation strategies to minimize the losses associated with 3D effects. A refined total loss model for the self-shielded inductor is derived.¹

4.1 Phi-directed Fields

Helical winding structures are often modeled in 2D as shown in Fig. 3-4 as rectangles for copper foil (circles in the case of copper wire winding) running parallel to each other. However, in real-life helical winding turns deviate from this idealized 2D model. Instead, the helical current results in a net z-directed current equal to the input current of the winding. This z-directed net current is shown in Fig. 4-1.

The presence of this z-directed current gives rise to phi-directed magnetic fields in the outer shell of the inductor (i.e., a field component oriented around the circum-

¹This model is based on the initial work done by Dr. Mike Ranjram in [2]

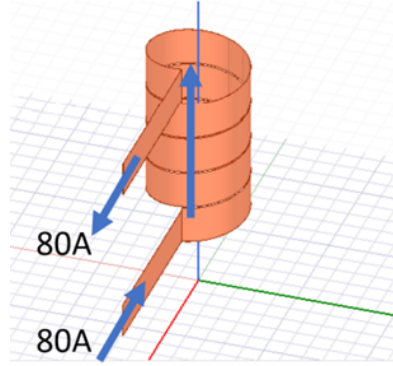


Figure 4-1: Net Z-directed current

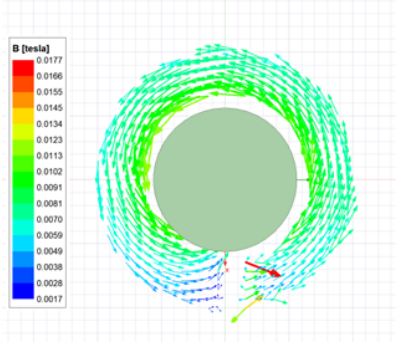


Figure 4-2: Phi-directed fields due to the Z-directed current in the design shown in Table 3.1

ference of the outer shell). These fields, however, cancel out in the center post. The initial self-shielded inductor design presented in [3][17] was based on a 2-D model analysis. the design results in a significant phi-directed field component in the outer shell, estimated to be 11mT as shown in Fig. 4-2; this is considerably large than the z-directed field component, measuring 3.5mT. This disparity in field strengths provides an explanation for the observed higher simulated core loss compared to what is anticipated from a 2D analysis as shown in Table 3.2. The phi-directed fields in the outer shell contribute significantly to core loss. Understanding and adequately modeling these phi-directed fields is important to assess and mitigate core loss in the design accurately.

4.1.1 Modeling Phi-directed Fields

We start by investigating the magnetomotive force (MMF) to develop an appropriate model for these phi-directed fields. The MMF generated by the z-directed current in the inductor winding creates a parallel path along each outer shell core piece and outer shell gap. As the outer shell has to have a minimum of one notch to accommodate the winding and allow it to pass through the core's window area as shown in Fig. 4-3. So for the reluctance model for a single shell piece, we consider two reluctances connected in series: one associated with the shell itself and another associated with the notch. This configuration is depicted in Fig. 4-4. The reluctance of a single shell core piece is denoted as $\mathcal{R}_{osc,\phi}$ can be calculated using the following equation:

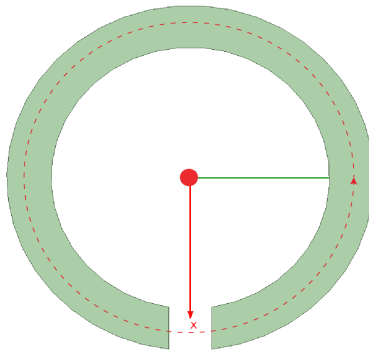


Figure 4-3: A single outer shell core piece

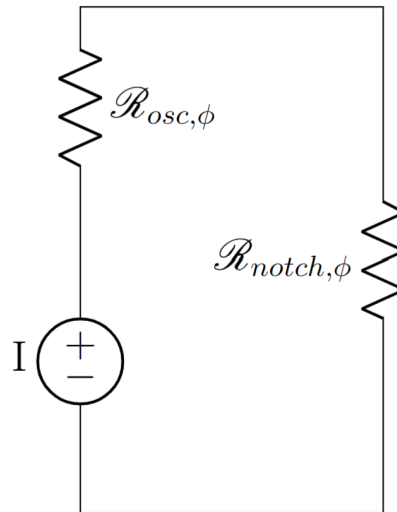


Figure 4-4: Magnetic circuit model for a single outer shell core piece

$$\mathcal{R}_{osc,\phi} = \frac{(2\pi - \alpha)(1 + c)R}{2\mu_0\mu_r h_{oc}} \quad (4.1)$$

In this equation, α represents the angular length of the notch in radians, $(1+c)R/2$ refers to the average radius of the shell, μ_0 denotes the permeability of free space, μ_r is the relative permeability of the core, and h_{oc} represents the thickness or height of the outer shell core piece. Similarly, we calculate $\mathcal{R}_{notch,\phi}$, the reluctance for the notch in the outer shell ring using the following equation:

$$\mathcal{R}_{notch,\phi} = \frac{\alpha(1 + c)R}{2\mu_0 h_{oc}} \quad (4.2)$$

The net phi-directed reluctance ($\mathcal{R}_{net,\phi}$) is expressed as the sum of the $\mathcal{R}_{osc,\phi}$ and $\mathcal{R}_{notch,\phi}$. The presence of phi-directed fields in the outer shell of the inductor contributes not only to core loss but also to the overall inductance of the structure. These fields, being orthogonal to the z-directed fields, store energy and affect the inductance characteristics. The inductance associated with the phi-fields (L_ϕ) can be defined as:

$$L_\phi = \frac{1}{\mathcal{R}_{net,\phi}} \quad (4.3)$$

	3-D ANSYS	Reluctance Model	Updated Reluctance Model
B_{phi} (mT)	11	8	10.8

Table 4.1: Predicted phi-directed field using reluctance models vs the phi-directed field seen in 3D ANSYS simulations

It was found from simulations that the current model underestimates the core loss caused by the phi-directed fields shown in Table 4.1. One reason for this is that the estimate of the notch reluctance is conservative, as it does not consider the increased cross-sectional area of the fringing path. This is particularly evident in cases where the shell gap height is much larger compared to the shell core thickness as shown in Fig. 4-5. To enhance the accuracy of the reluctance model and address any potential limitations in the design optimization process, adjustments are made to incorporate

the fringing fields present in the outer shell gaps. The model is updated to include two parallel reluctances for the notch: one related to the shell thickness (already accounted for in the model above) and another related to the gap thickness using equation (4.4). This modification significantly improves the matching of core loss. The updated reluctance model is shown in Fig. 4-6.

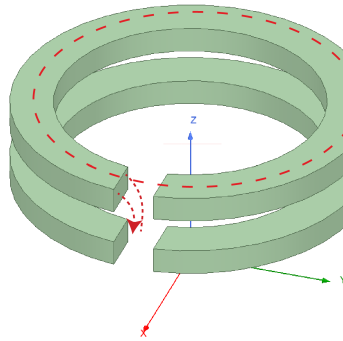


Figure 4-5: Stack of outer shell core pieces

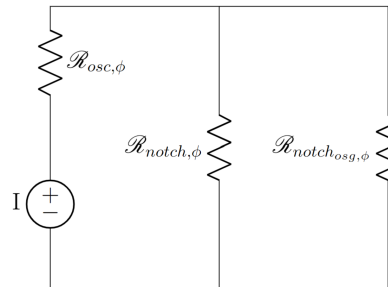


Figure 4-6: Magnetic circuit model for a single outer shell core piece accounting for the fringing field through the shell gap

$$R_{notch_{og},\phi} = \frac{\alpha(1+c)R}{2\mu_0 h_{og}} \quad (4.4)$$

Where, h_{og} is the height of the outer shell gap.

4.1.2 Mitigating Phi-directed Fields

Now that we have a reliable model to estimate the impact of phi-directed fields, we can utilize it to optimize the design and minimize the overall loss in the inductor. The presence of phi-directed fields is a geometrical phenomenon, and therefore, exploring geometrical modifications to the design can help mitigate the losses associated

with these fields. Two main strategies to address the issue of phi-directed fields and minimize their impact are explored.

Phi-directed quasi-distributed gaps to increase reluctance

One effective approach for mitigating phi-directed fields involves increasing the reluctance of the phi-field path. One way to achieve this is by increasing the length of the notch in the outer shell, which serves as the entry and exit point for the winding. However, implementing a single large notch can have disadvantages, as discussed in Chapter 3.

We need to address the possibility of fringing fields from the notches causing proximity effect loss in the windings. We do this by incorporating quasi-distributed gaps in the outer shell. By strategically placing gaps along the outer shell, the path for phi-directed magnetic flux is interrupted, leading to an increase in reluctance. These quasi-distributed gaps can be implemented symmetrically, distributing the interruption of the phi-field path evenly throughout the outer shell. This approach helps reduce the intensity of the phi-directed fields and their associated core losses. However, it is important to consider the trade-off that increasing the length of these gaps may result in a reduction of the cross-sectional area available for z-directed fields within the outer shell.

To estimate this tradeoff, we sweep the total notch angle for an approximately 500nH example self-shielded inductor design and evaluate its effect on the inductance and the losses in the inductor. The notch angle is swept from 30° to 90° . From Fig. 4-7 it is evident that as the notch angle increases, both the copper loss and core loss experience a significant reduction. This core loss reduction can be attributed to reduced phi-directed field magnitude as we increase the reluctance for the phi-directed path. We also see copper loss going down as the notch angle increases. This can be attributed to the increase in the free space around the winding terminal as it minimizes current crowding in those areas. However, it should be noted that increasing the notch angle also leads to a reduction in the available area for the z-directed field, resulting in a degradation of inductance. Based on the performance

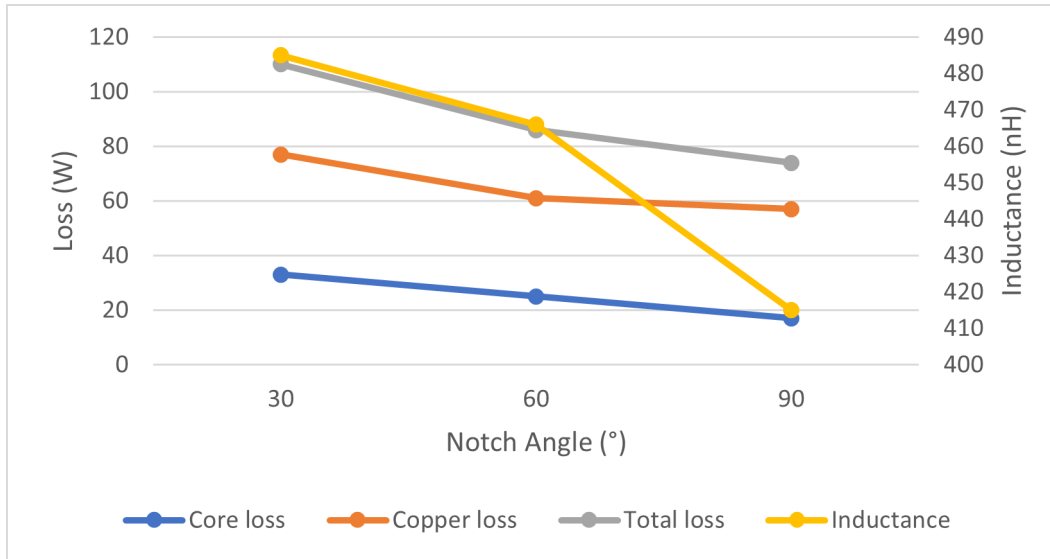


Figure 4-7: Inductor inductance and performance vs notch angle

analysis, the optimal design is observed at a notch angle of 60° , which allows for a 7% degradation in inductance. This design strikes a balance between minimizing total losses i.e. maximizing Q, considering the acceptable level of inductance degradation.

Winding configuration to eliminate Z-directed current

Another strategy to mitigate the phi-directed fields and the associated core loss is to eliminate the z-directed currents that give rise to these fields. This approach focuses on modifying the winding configuration or structure of the inductor. There are a number of interesting possibilities for simply removing net Z-directed current some of them are explored below.

One such possibility is to provide a return path for the winding (Fig. 4-8) inside the outer shell to eliminate or minimize the net z-directed current and the associated phi-directed fields and core losses. By incorporating a dedicated pathway for the return current within the outer core, the overall magnetic flux distribution is balanced, resulting in zero net z-directed current. The notch space in the outer shell can be used to house this return path. However, this configuration increases copper loss due to proximity between the input and output terminals and can increase the capacitance of the inductor.

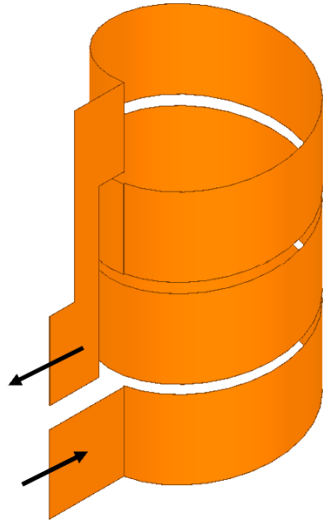


Figure 4-8: Helical winding with a return path through the notch : minimizes z-directed current

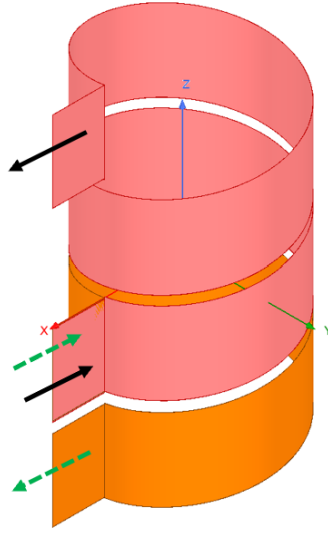


Figure 4-9: Winding split into two halves with z-directed currents in opposite direction: minimizes z-directed current

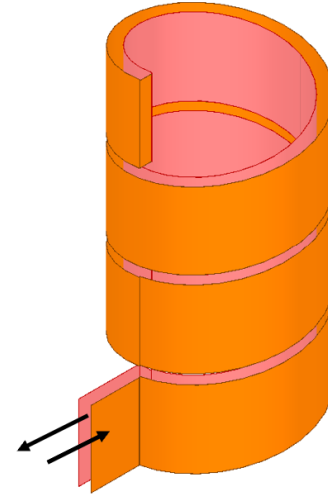


Figure 4-10: Double layer winding : eliminates z-directed current

Another possibility is to split the coil into two mirrored halves (Fig. 4-9), where the upper portion carries a net positive z-directed current and the lower portion carries a net negative z-directed current. This configuration maintains the excitation of the z-directed field while halving the phi-directed fields for the same core geometry. Consequently, core losses associated with the phi-directed fields are dramatically reduced. However, this construction introduces an additional termination region to the structure, which can complicate its connection to the outside world.

Alternatively, another construction involves winding the helix in two layers, with one layer wound "up" and the other layer wound "down" (Fig. 4-10). This arrangement completely eliminates the z-directed fields. However, implementing a two-layer structure significantly increases the capacitance of the system, and can also significantly increase copper loss which can have detrimental effects on performance.

4.1.3 Mitigation Strategy Comparison

To validate the relative effectiveness of the mitigation strategies, a comparison was conducted among three different 500nH inductor designs: A, B, and C as shown in Fig. 4-11. The results highlight the impact of these strategies on the magnitude of phi-directed fields. Here's a summary of the findings:

- Inductor A (original design): This design featured a net z-directed current of 80A, which generated a significant phi-directed magnetic field magnitude of 11mT in the outer shell pieces. The z-directed field component measured 3.5mT.
- Inductor B (Mitigation strategy 1): In this design, notches were introduced in the outer shell pieces to mitigate the phi-directed fields resulting from the net z-directed current. By incorporating a quasi-distributed 60-degree notch configuration, the magnetic field magnitude in the outer shell pieces was reduced by a factor of 2 compared to Inductor A.
- Inductor C (Mitigation strategy 2): The winding configuration in this design involved a return path through the outer shell notch gap, effectively eliminating the net z-directed current within the outer shell structure. As a result, the magnitude of the phi-directed field was significantly reduced to 0.3mT.

These findings validate the effectiveness of the mitigation strategies in reducing the phi-directed field magnitudes. Inductor B demonstrated a notable reduction compared to the original design, while Inductor C achieved a remarkable decrease by eliminating the net z-directed current entirely. These results support the notion that the mitigation strategies effectively address the issue of phi-directed fields and their associated core losses.

4.2 End-Turns Effect

The helical nature of the coil introduces an important aspect called "asymmetry" in how the circular core pieces are arranged compared to the evolution of the helical

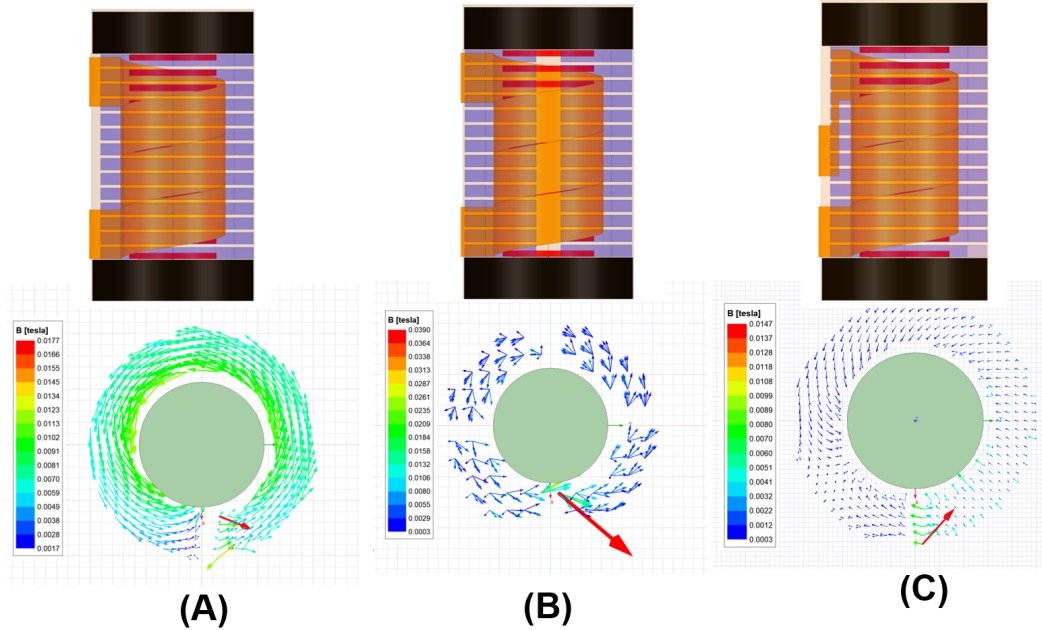


Figure 4-11: Impact of mitigation strategies on the phi-directed fields for 500 nH self-shielded inductor designs (A) Inductor design details in Table 3.1 (B) Design in A with outer shell modification total notch angle = $\frac{\pi}{3}$ (C) Design in A with a winding return path (z-distance between input and output terminals = 10 mm)

winding through the window. In a 2D analysis, individual turns of the winding can be identified and discussed, and their z-directed displacement remains constant throughout, similar to the core structure.

However, in a 3D analysis, the turns of the winding are displaced in the z-direction by their height, and an additional spacing between turns (e.g., 1mm). This displacement becomes particularly significant at the ends of the windings, altering the path of magnetic flux through this region. It also leads to current-crowding effects, where the magnetic fields jump across the winding window.

This phenomenon of z-directed turn displacement and current-crowding introduces additional complexities in the magnetic behavior and distribution within the winding structure. It affects how the flux travels through the winding ends and influences the overall performance and characteristics of the inductor. Therefore, accounting for these 3D effects is crucial for a more accurate analysis and design optimization of the helical inductor.

4.2.1 Modeling Lost Gaps

We investigate the z-directed flux paths and the magnetic field distribution at the end of the winding to understand the impact of the end-turns effect. Figure 4-12 illustrates the magnitude of the H-field on the YZ cross-section of an example 500 nH self-shielded inductor. As we move from the top to the bottom on the left side of the inductor, we observe a gradual weakening of the H-field in the gaps. This weakening continues until the H-field becomes nearly zero for the bottom three gaps. Similarly, as we move from the bottom to the top on the right side, we observe a similar weakening of the H-field. This behavior indicates that the magnetic field is jumping across the window near the ends of the winding. This decreases the net reluctance of the core as some of the gaps are being bypassed. Thus, resulting in higher inductance in combination with additional inductance coming from phi-directed fields. This phenomena explains the discrepancy between the simulated inductance (790nH) and the designed inductance (500nH) in Table 3.2.

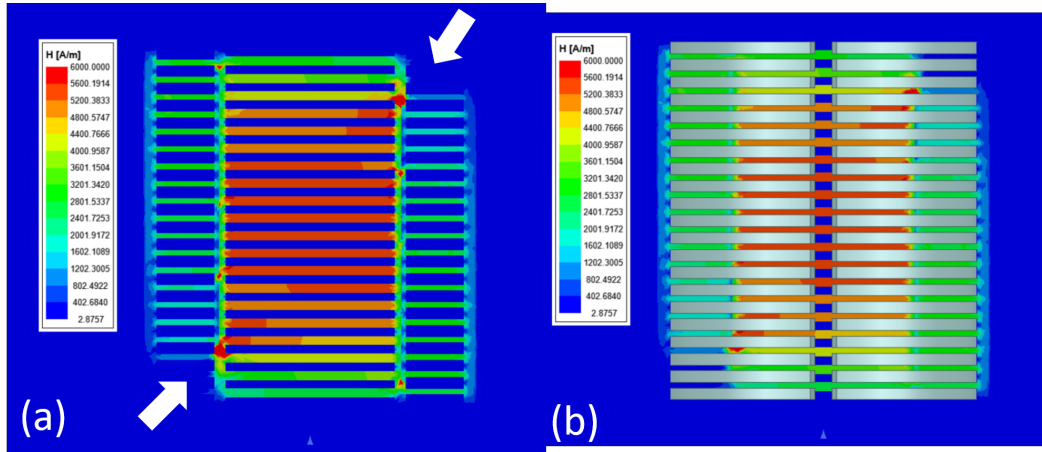


Figure 4-12: H-field distribution on the YZ Cross-Section of a self-shielded Inductor, design details in Table. 3.1, highlighting the tendency of fields to bridge the winding gap near the window ends. (a) Unobstructed view highlighting 'lost gaps' with arrows. (b) Core shell locations included for reference.

To model the phenomenon of flux jumping across the winding window, we account for the possible paths that the magnetic field can take. Assuming that the only viable path is through the non-conductive portions of the window, we update the model by

including reluctances associated with the "r-directed" window paths. This is under the assumption that the winding rejects flux attempting to pass through it. The height of the region where fields can jump the window varies with the position of the helix, as depicted in Fig. 4-13. The effective reluctance associated with this window-jumping path is determined by the following equation:

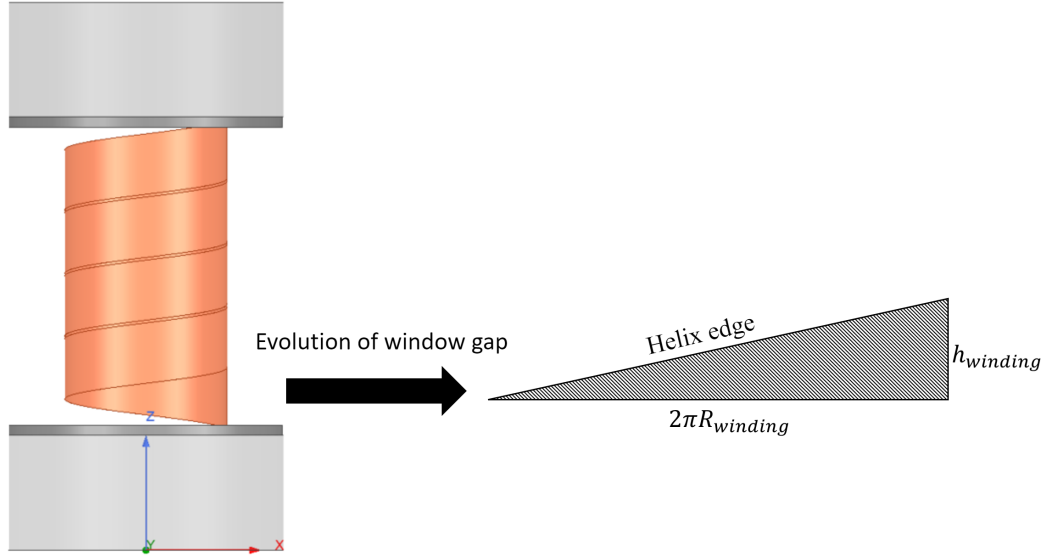


Figure 4-13: Window gap reluctance estimation

$$\mathcal{R}_{window} = \frac{(c - b)R}{\mu_0 A_{wg,eff}} \quad (4.5)$$

Here, $(c - b)R$ represents the height of the window gap, and R is the radius of the end cap. The effective area of this path is given by:

$$A_{wg,eff} = \pi R_{winding} h_{winding} = \pi h_{winding} \left(\frac{c + b}{2} R \right) \quad (4.6)$$

Therefore, the expression for the window reluctance becomes:

$$\mathcal{R}_{window} = \frac{2}{\mu_0 \pi h_{winding}} \left(\frac{c - b}{c + b} \right) \quad (4.7)$$

We consider that this reluctance is connected in parallel with the number of outer core pieces and outer core gaps encompassed within the height of one winding. The

number of lost gaps, $N_{g,lost}$, can be expressed as:

$$N_{g,lost} = \frac{h_{winding}}{h_{og} + h_{oc}} \quad (4.8)$$

Therefore, instead of considering the full reluctances of the outer core and outer gaps, we use a modified reluctance model illustrated in Fig. 4-14. This model represents the main shell pieces, endplate pieces, and the final shell pieces connected in parallel with the gap. By incorporating the concept of lost gaps, we can more accurately estimate the inductance for the design.

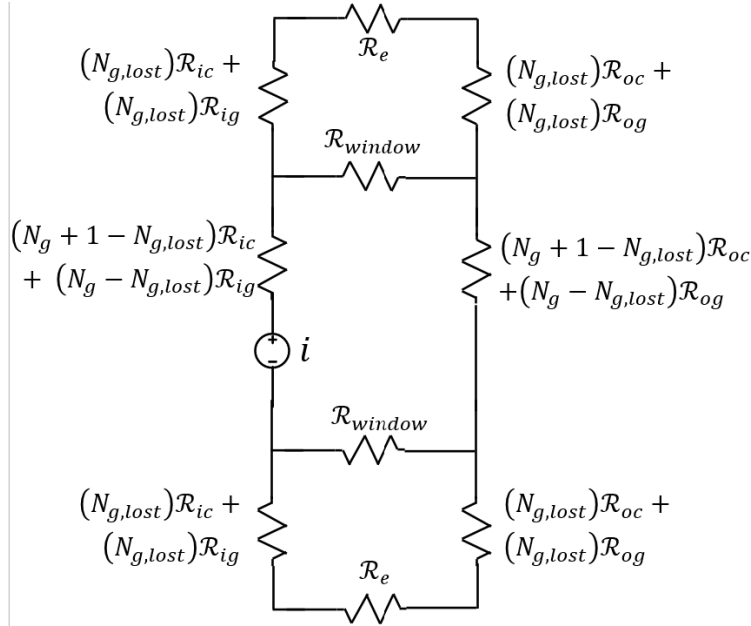


Figure 4-14: Modified magnetic circuit model for z-directed fields that accounts for the additional reluctance due to lost gaps

Where, i is the excitation current, \mathcal{R}_{ic} is the reluctance of inner core piece in the z-direction, \mathcal{R}_{ig} is the reluctance of inner gap piece in the z-direction, \mathcal{R}_{oc} is the reluctance of outer core shell piece in the z-direction, \mathcal{R}_{og} is the reluctance of outer shell gap piece in the z-direction. N_g is the total number of gaps in the inner core section (equal to number of outer gaps). $N_{g,lost}$ is the number of gaps that compete with window reluctance path. \mathcal{R}_{window} and \mathcal{R}_e are the reluctances of the window path and the endplate respectively.

4.2.2 End Cap Flux Imbalance

The analysis of the endcap regions in Fig. 4-15 reveals a similar phenomenon, where the B-field is preferentially concentrated on one side of the core, indicating that the other part of the endcap carries minimal flux. This observation aligns with the notion of fields jumping across the gap. Furthermore, the Fig. 4-15 also shows a radial dependency of the B-field localized in the region of the core affected by phi-fields. However, it's important to note that this phenomenon is related to the phi-fields and not the z-fields.

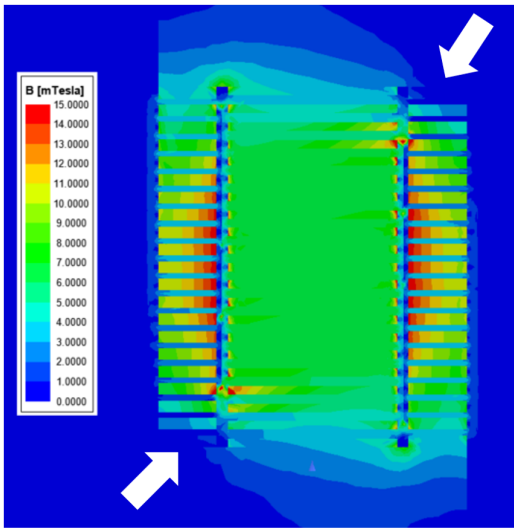


Figure 4-15: B-field distribution on the YZ Cross-Section of a self-shielded Inductor, highlighting the field imbalance in endcaps and radial dependency due to Phi-directed fields. Lost gaps marked with arrows.

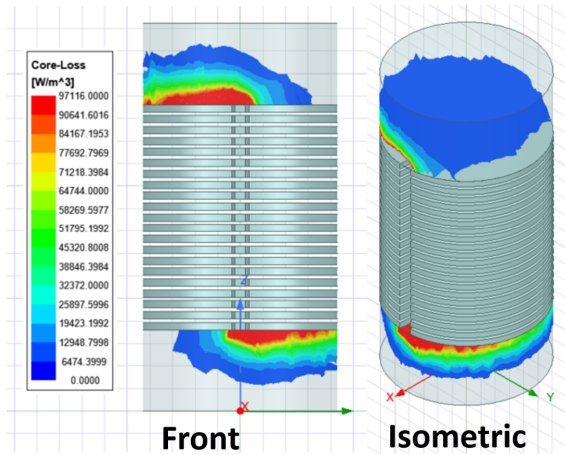


Figure 4-16: Core loss distribution in the top and bottom endcap confirming that flux imbalance in end caps due to end turns effect

Given our assumptions regarding flux jumping across the window, we estimate the flux inside the endplates by considering the flux that does not cross the gap. Although the simulation results in Fig. 4-16 indicate that the entire volume of the endcaps may not be fully utilized, for the purpose of modeling, we make a crude assumption that it is. Since the endcaps are not gapped, they have a minimal effect on the inductance. Therefore, their height can be adjusted based on the simulated core loss in the endplate. As a result, developing a refined model specifically for this

loss component is relatively less crucial.

4.2.3 Current Crowding

The presence of radial fields across the window lead to current crowding at the edges of the winding. The MMF that is dropped across the equivalent "window jumping" reluctance Fig. 4-14 is responsible for driving losses at the winding edges. However, it is challenging to determine the portion of this MMF that impacts the edge of the winding accurately, as the window width is much larger than the thickness of the winding. Developing a precise model for this effect is complex, however, accounting for some level of current crowding is important. It was observed from simulation results that the refined loss model even after accounting for phi-directed fields and lost gaps was underestimating the copper loss in the winding by a factor of 1.6. The simulations accounted for the skin effect loss in the winding so this discrepancy likely comes from the current crowding loss in the winding caused by the radial flux.

4.3 Conclusion

The modified inductor design accounting for the 3D effects of the low-turn winding is shown in Fig. 4-17. The key dimensions that parameterize the design are labeled in the figure. The outer shell rings have distributed gaps in the phi-direction to mitigate phi-directed field losses. While providing a return path for the winding, as discussed earlier, can help eliminate phi-directed field losses, modeling the proximity losses between the winding and its return path poses a significant challenge. Therefore, this feature will be further evaluated directly through simulations in the following chapter. By incorporating insights gained through the modeling of the phi-directed path reluctance and lost gaps due to the end turns effect, we develop an improved model that provides more accurate predictions for the total loss and inductance of the inductor.

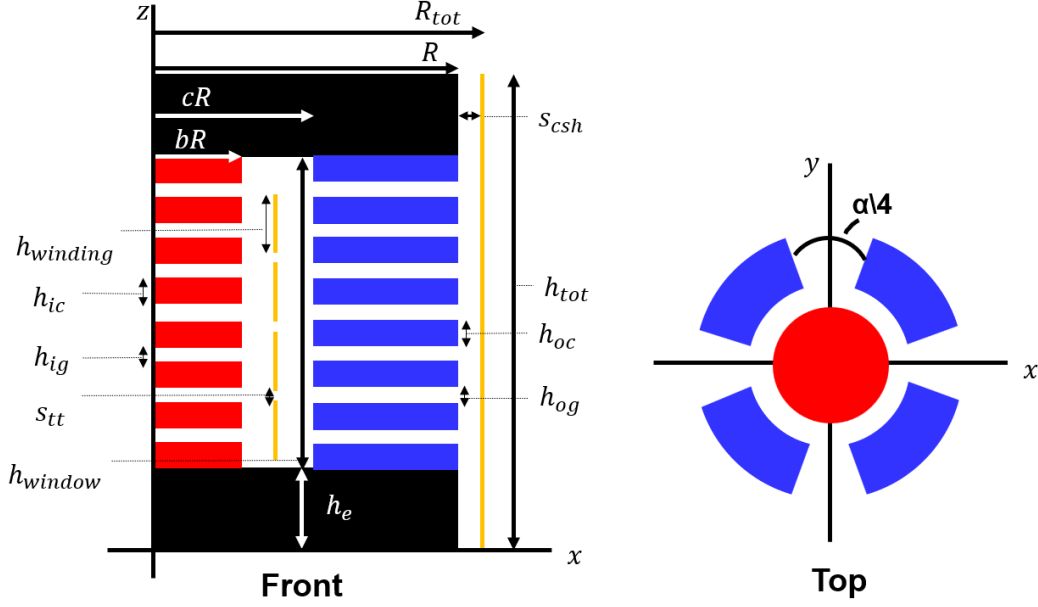


Figure 4-17: Front view and top view of the proposed inductor design with geometrical parameters

4.3.1 Refined Loss Model

To develop a refined loss model, we follow the same steps as shown in section 3.3. The total loss in the inductor is the sum of the core loss and the copper loss as shown below :

$$\text{LOSS} = P_{\text{core,center}} + P_{\text{core,shell}} + P_{\text{core,end caps}} + P_{\text{winding,inner}} + P_{\text{winding,outer}} + P_{\text{shield}} \quad (4.9)$$

Reluctances of center post and outer shell are updated to account for the reduced reluctance due to lost gaps at the ends as discussed in subsection 4.2.1. Even though we established in subsection 4.2.2 that the entire area of the end caps is not being utilized. To keep the model simple we operate under the assumption that it is and the reluctance of the end caps remains the same as in the 2D model :

$$\mathcal{R}_{\text{center}} = \frac{h_w}{\mu_{\text{rec}}\mu_0\pi b^2 R^2} - N_{g,\text{lost}}(h_{ic} + h_{ig}) \quad (4.10)$$

$$\mathcal{R}_{\text{shell}} = \frac{h_w 2\pi}{\mu_{res} \mu_0 \pi R^2 (1 - c^2) (2\pi - \alpha)} - N_{g,lost} (h_{oc} + h_{og}) \quad (4.11)$$

$$\mathcal{R}_{\text{end cap}} = \frac{(1 + c)}{\mu_r \mu_0 \pi 2h_e} \quad (4.12)$$

Where, $N_{g,lost}$ is the number of lost gaps at the ends and is calculated using equation (4.8). $h_{ic}, h_{ig}, h_{oc}, h_{og}$ are the heights of the core piece and the gaps for the center post and the outer shell respectively. μ_{rec} and μ_{res} can be found from equation (3.4) and μ_r is the relative permeability of the core material. α is the total notch (gap) angle in the outer shell ring. Next, we estimate the reluctance for the flux that doesn't escape and manages to go through the lost gaps.

$$\mathcal{R}_{\text{lostpath}} = \frac{N_{g,lost}}{2} \left(\frac{h_{ic}}{\mu_r \mu_0 \pi b^2 R^2} + \frac{h_{ig}}{\mu_0 \pi b^2 R^2} + \frac{h_{oc} 2\pi}{\mu_r \mu_0 \pi R^2 (1 - c^2) (2\pi - \alpha)} + \frac{h_{og} 2\pi}{\mu_0 \pi R^2 (1 - c^2) (2\pi - \alpha)} \right) \quad (4.13)$$

This reluctance in parallel with the $\mathcal{R}_{\text{window}}$ presented in equation (4.7) accounts for the flux that flows through the lost path and the window gap.

$$\mathcal{R}_{\text{window,lostpath}} = \mathcal{R}_{\text{window}} || \mathcal{R}_{\text{lostpath}} \quad (4.14)$$

Inductance due to the z-directed field is calculated as :

$$L_z = \frac{N^2}{\mathcal{R}_{\text{center}} + 2\mathcal{R}_{\text{shell}} + \mathcal{R}_{\text{end cap}} + 2\mathcal{R}_{\text{window,lostpath}}} \quad (4.15)$$

The MMF drop across $\mathcal{R}_{\text{center}} : \mathcal{F}_{\text{inner}}$, it will be the sum of the MMF drop due to the flux in the center post plus the flux drop due to the flux through the lost path and MMF across $\mathcal{R}_{\text{shell}} : \mathcal{F}_{\text{outer}}$.

$$\mathcal{F}_{\text{inner}} = \frac{L_z I \mathcal{R}_{\text{center}}}{N} + \frac{L_z I}{N} \frac{\mathcal{R}_{\text{window}}}{\mathcal{R}_{\text{lostpath}} + \mathcal{R}_{\text{window}}} \left(\frac{h_{ic}}{\mu_r \mu_0 \pi b^2 R^2} + \frac{h_{ig}}{\mu_0 \pi b^2 R^2} \right) \quad (4.16)$$

$$\mathcal{F}_{\text{outer}} = NI - \mathcal{F}_{\text{inner}} - \frac{2\mathcal{R}_{\text{end cap}}L_z I}{N} \quad (4.17)$$

$$P_{\text{winding,inner}} = \frac{1}{2} \left(\frac{\rho_{\text{cu}}}{h_{\text{winding}}} \frac{2\pi bR}{\delta} \right) \mathcal{F}_{\text{inner}}^2 \quad (4.18)$$

$$P_{\text{winding,outer}} = \frac{1}{2} \left(\frac{\rho_{\text{cu}}}{h_{\text{winding}}} \frac{2\pi cR}{\delta} \right) \mathcal{F}_{\text{outer}}^2 \quad (4.19)$$

$$P_{\text{shield}} = \frac{1}{2} \left(\frac{\rho_{\text{cu}}}{h_{\text{tot}}} \frac{2\pi R_{\text{tot}}}{\delta} \right) \mathcal{F}_{\text{outer}}^2 \quad (4.20)$$

The magnetic field density is evaluated in the core pieces to estimate the core loss using the Steinmetz equation [20]. In the 2D model, it is assumed that the magnetic field density is the same for all the core pieces. However, this is not the case in reality. In this model, the flux density is evaluated for the center post and the core pieces at the end that account for the lost path separately.

$$B_{\text{center}} = \frac{L_z I}{N\pi b^2 R^2} \quad (4.21)$$

$$B_{\text{center,lostpath}} = \frac{L_z I}{N\pi b^2 R^2} \frac{\mathcal{R}_{\text{window}}}{\mathcal{R}_{\text{lostpath}} + \mathcal{R}_{\text{window}}} \quad (4.22)$$

$$B_{\text{shell}} = \frac{L_z I 2\pi}{N\pi(1 - c^2)R^2(2\pi - \alpha)} \quad (4.23)$$

$$B_{\text{shell,lostpath}} = \frac{L_z I 2\pi}{N\pi(1 - c^2)R^2(2\pi - \alpha)} \frac{\mathcal{R}_{\text{window}}}{\mathcal{R}_{\text{lostpath}} + \mathcal{R}_{\text{window}}} \quad (4.24)$$

$$B_{\text{end cap}} = \frac{L_z I}{N\pi R h_e} \quad (4.25)$$

The expressions for calculating the core losses in the center post, outer shell, and end cap of the inductor are as follows:

$$P_{\text{core,center}} = (N_g + 1 - N_{g,\text{lost}})C_m f^\alpha B_{\text{center}}^\beta \pi b^2 R^2 h_{ic} + N_{g,\text{lost}})C_m f^\alpha B_{\text{center,lostpath}}^\beta \pi b^2 R^2 h_{ic} \quad (4.26)$$

$$P_{\text{core,shell}} = (N_g + 1 - N_{g,\text{lost}})C_m f^\alpha B_{\text{shell}}^\beta \pi (1 - c^2) R^2 \frac{(2\pi - \alpha)}{2\pi} h_{oc} + N_{g,\text{lost}})C_m f^\alpha B_{\text{shell,lostpath}}^\beta \pi (1 - c^2) R^2 \frac{(2\pi - \alpha)}{2\pi} h_{oc} \quad (4.27)$$

$$P_{\text{core,end caps}} = 2C_m f^\alpha B_{\text{shell}}^\beta \pi R^2 h_e \quad (4.28)$$

C_m , α and β are Steinmetz parameters for the core material and can be extracted from the datasheet for a frequency of interest. N_g is the total number of gaps in the center post and outer shell.

4.3.2 Results

The refined loss model discussed above is used to predict the loss in the inductor from Table 3.2. The loss predicted from the refined model-based MATLAB script is compared to 3-D ANSYS finite element analysis (FEA) simulation as shown in Table 4.2. The findings show reasonable agreement between the Model predictions and 3D simulation results, with the model slightly underestimating copper loss. This is potentially due to the lack of a well-defined model of current crowding at the ends. The reasonable match between the model predictions and simulation results provides credence to the validity of the refined model.

	2-D Model	2-D ANSYS	3-D ANSYS	Refined Model
Inductance (nH)	500	623.45	790	760
Copper Loss (W)	56.21	63.81	102	80
Core Loss (W)	32.57	46.31	191	179
Total Loss (W)	88.69	110.1	273	259

Table 4.2: Comparison between the refined model-based prediction and 3D ANSYS simulations of the Self-Shielded Inductor Structure

Chapter 5

An example 500 nH design

In this section, we will outline a sample design for a 500 nH inductor utilizing the design guidelines from Chapter 3 and the improved model from Chapter 4 to achieve an optimized design. The performance of this design will be evaluated in ANSYS MAXWELL 3D and its thermal viability will be assessed using ANSYS ICEPAK.

5.1 Optimizing Inductor Design

The objective is to minimize the overall loss function, as established in Chapter 4, given a specific inductance value and the total inductor volume. To make the optimization easier and reduce the degrees of freedom, we input some parameters into the system. The inductance is set to 500 nH and the total volume of the inductor is confined to $2L$. The operation frequency and the peak of the sinusoidal current flowing through the inductor are 13.56 MHz and 80 A, respectively. Fair-rite's 67 ($\mu_r = 40$) material was selected as the core material due to its exceptional performance factor at the frequency of operation [9, 3]. A $50 \mu m$ thick copper foil was selected as the winding to allow for up to 3 skin depths of conduction area at 13.56 MHz. It is assumed that the center post and the outer shell have the same number of gaps to limit the degrees of freedom.

We developed a MATLAB script (refer to Appendix B) that employs a brute-force approach to search the parameter space and optimize the total loss for the given

input parameters. The script optimizes the design by iteratively testing and refining different configurations, ensuring that the proposed design not only minimizes total loss but also meets the practical requirements of an inductor set by some specific constraints discussed below.

5.1.1 Design Constraints

Before finalizing a design, it is essential to ensure that it meets all the specified constraints. This includes the pitch-to-spacing constraint mentioned earlier in 3.2.2 [10]. Additionally, the window area must be sufficient to accommodate the winding, and all other dimensions should be physically feasible. Lastly, the two other crucial constraints are the self-resonant frequency of the inductor and the maximum magnetic flux density in the core.

Self-Resonant Frequency (SRF)

The design constraints require that the SRF be greater than 54MHz, which is four times the operating frequency. The SRF of the shielded inductor is approximated using Knight's formula [14]. The formula assumes internal and external permittivity defined by the effective permittivity of the inner post and the outer shell, respectively.

Maximum Magnetic Flux Density

The 67 material, selected in our inductor design, offers several benefits that enhance its overall performance. It provides lower losses even at higher frequencies, contributing to the efficiency of the inductor in these frequency ranges. Furthermore, it exhibits a more stable response over a range of temperature variations, ensuring a consistent and reliable performance irrespective of thermal conditions.

However, it's worth noting that the 67 material, being a perminvar substance, does have one significant drawback. It has a tendency to experience irreversible changes in permeability and losses when exposed to intense magnetic fields, even those well below its saturation limit, or under conditions of excessive mechanical stress. As indicated

in [4], the 'whapping' threshold at 13.56 MHz is approximately 22 mT. Therefore, it's crucial to constrain the maximum B field in the core pieces to be less than this threshold. Exceeding this limit could induce irreversible changes to the power loss curve of the 67 material, adversely affecting the performance and reliability of the inductor over time.

5.1.2 Optimized Design Details

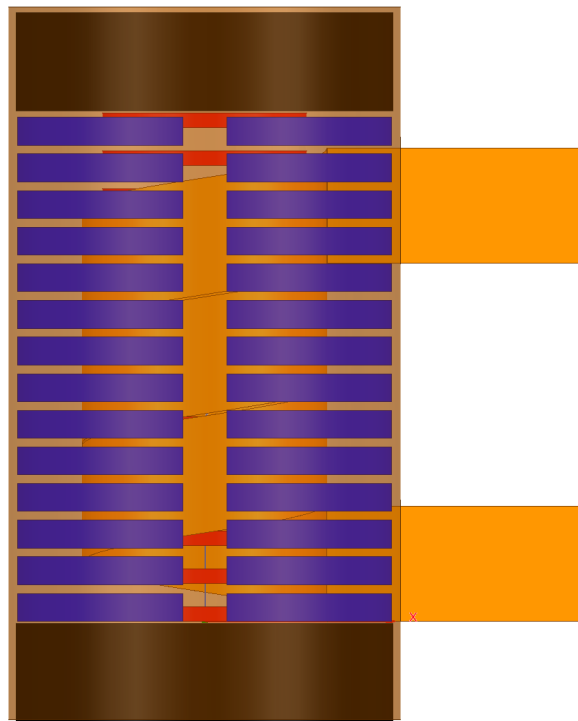


Figure 5-1: Side view of the optimized self-shielded inductor design. End-caps shrunk based on 5.2.2

An optimized inductor design is obtained that has the minimum total loss for the given design constraints. The inductor structure is shown in figure 5-1¹. The key dimensions and details of the optimized design are listed in Table 5.1.

¹The total height of the center post and outer shell is slightly different due to the difference in available non-magnetic spacer material thicknesses for their respective gaps.

Volume	2L
Inductance	500 nH
End-cap radius	51 mm
Center-post radius	27.7 mm
Outer-shell inner radius	38.64 mm
Winding radius	33.24 mm
Shield radius	51.92 mm
End-cap height	53.36 mm
Total height	236 mm
Number of gaps	13
Number of turns	3
Center-post core piece height	3.927 mm
Outer-shell core piece height	7.527 mm
Winding foil height	31.21 mm
Winding turn-to-turn spacing	1 mm
Winding foil thickness	50 μ m
Total notch angle in outer shell	$\pi/3$
Number of notches	4
Core material	Fair-rite 67

Table 5.1: Geometry of the optimized self-shielded inductor.

5.2 ANSYS 3D Simulations

The optimized inductor design is simulated in ANSYS MAXWELL 3D. The operating frequency is set to 13.56 MHz and the current through the inductor is set to 80 A. The simulation results, which include measurements of the inductance and total loss within the inductor, are presented in Table 5.2, a detailed loss breakdown is shown in Fig. 5-3. The inductor is predicted to achieve a high Q of 1495.

Inductance	470 nH
Total loss	85 W
Q	1495

Table 5.2: Simulated losses in the optimized 500nH self-shielded inductor

Figure 5-2 illustrates the simulated B-field distribution within the center post, outer shell, and end caps. The B-field is well below 20mT, a crucial threshold to pre-

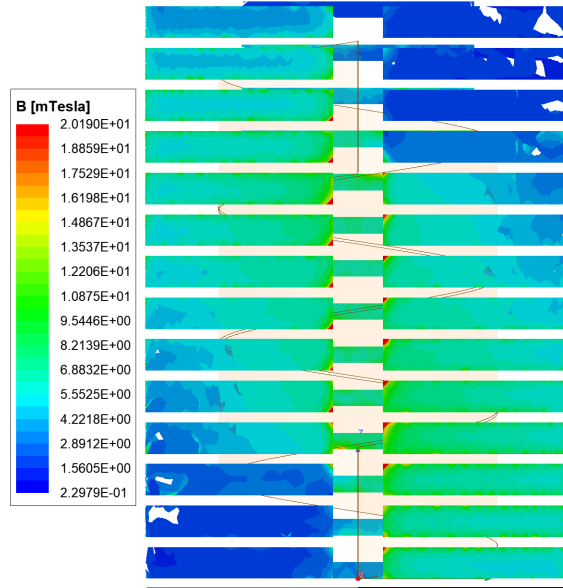


Figure 5-2: B-field distribution in outer shell and center post for the optimized inductor design. Below 20 mT to avoid whapping.

vent the "whipping" of the ferrite core pieces. It's observed that the B-field intensity exceeds this threshold at the edges of the outer shell pieces adjacent to the winding's entry and exit points. However, as this region is relatively small compared to the total area, the risk of whapping isn't a significant concern.

The non-uniformity in B-field distribution seen in Fig. 5-2 is a result of the 3D effects discussed in Chapter 4 and is particularly noticeable due to the low turn count ($N=3$) in the inductor design. The B-field intensity is lower in the core pieces at the ends, which can be attributed to the lost gap, i.e., the field jumping the window. Furthermore, the B-field exhibits a radial dependence, which indicates the presence of a phi-directed field. The loss analysis, as presented in the Fig. 5-3, underscores that the core loss in the outer shell is indeed the primary loss contributor. This loss is largely driven by the phi-directed field component. While the current design achieves a commendably high Q , we attempt to explore potential design modifications that could further minimize these phi-directed fields, without tampering with the already optimized parameters.

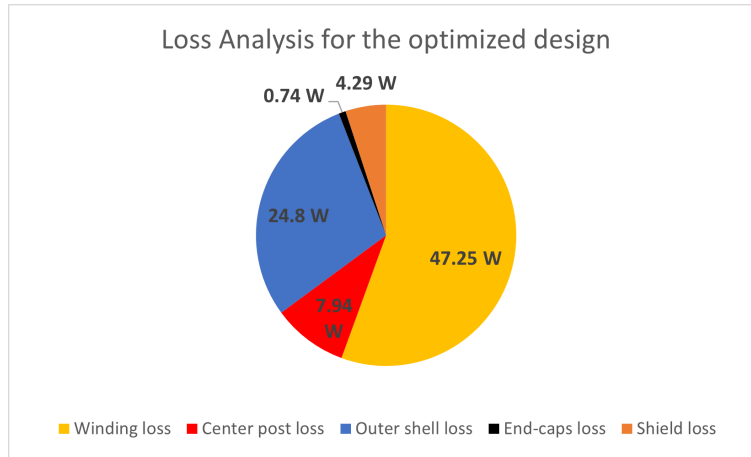


Figure 5-3: Loss distribution in the optimized inductor. Total loss = 85 W.

5.2.1 Winding Return Path Modification to Minimize Loss

Our design already incorporates notches into the outer shell rings, aiming to minimize the strength of the phi-directed fields, which causes loss in the outer shell. As established in Chapter 4, the phi-directed field losses in the outer core can be appreciably mitigated by introducing a return path for the winding inside the outer shell. This integration increases proximity loss in the winding and is difficult to model. Hence, we directly modify our optimized design outlined above by providing a return path for winding through one of the outer shell notches as shown in Fig. 5-4. The simulation results for this modified design are shown in Fig. 5-5 and compared to the original optimized design which only uses notches for mitigating phi-directed fields. The loss comparison chart demonstrates that although adding a return path for the winding reduces outer shell core loss by 50%, the total copper loss increases significantly. Consequently, the overall loss reduction in the inductor is less than 10%.

To simplify the design and manufacturing process of this example inductor, we have decided to stick with the optimized design that incorporates notches. The reduction in loss achieved by using a return path for the winding is not significant enough to justify the added complexity and challenges in modeling and manufacturing.

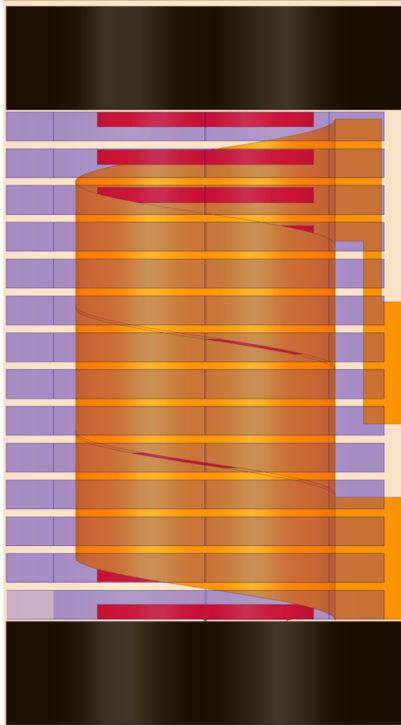


Figure 5-4: Self-shielded cored inductor simulation with a return path for winding. Design details in Table 5.3. The distance between the return path and the winding was optimized through sweep in simulations. Z-displacement between input and output terminal = 20 mm, radial distance between return path and winding = 7 mm

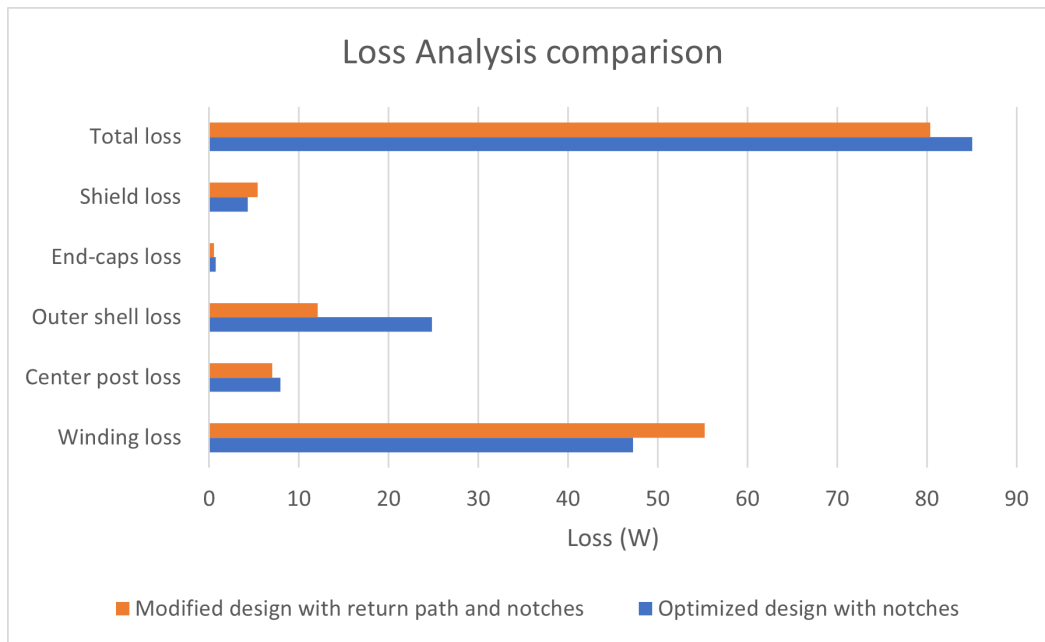


Figure 5-5: Loss analysis comparison for optimized design with and without return winding path

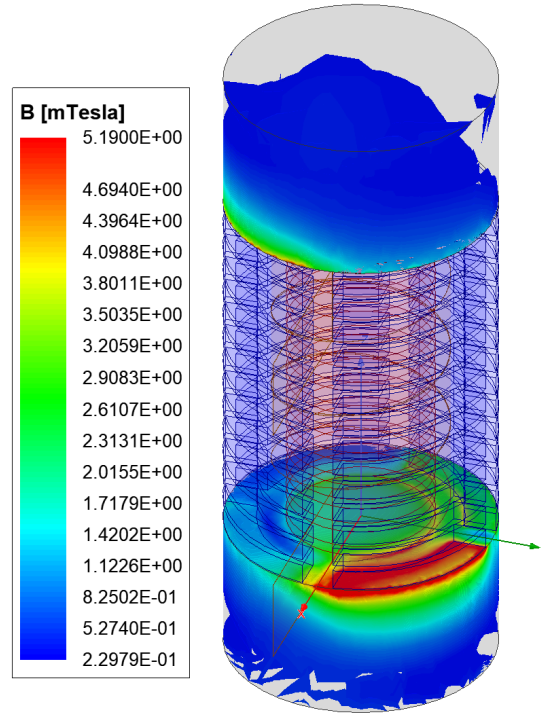


Figure 5-6: B-field distribution in end-caps suggest they are oversized

5.2.2 End-Cap Shrinking to Reduce Size

In Fig. 5-6, the B-field distribution in the top and bottom end-cap of the inductor is depicted. As explained in Chapter 4, there is an imbalance in the field distribution caused by the field jumping the window. The end caps are oversized and can be shrunk in thickness to reduce the volume of the inductor. In order to determine the extent to which the end caps can be shrunk without compromising the inductor's performance, a sweep analysis was conducted in ANSYS. It was observed that the height of the end caps can be safely reduced by a factor of 2 without impacting the inductance or total loss of the inductor. Thus, the volume of the inductor is reduced from $2L$ to $1.6L$. The updated self-shielded inductor geometry parameters after shrinking end caps is shown in Table 5.3.

Volume	1.6L
Inductance	500 nH
End-cap radius	51 mm
Center-post radius	27.7 mm
Outer-shell inner radius	38.64 mm
Winding radius	33.24 mm
Shield radius	51.92 mm
End-cap height	26.63 mm
Total height	192 mm
Number of gaps	13
Number of turns	3
Center-post core piece height	3.927 mm
Outer-shell core piece height	7.527 mm
Winding foil height	31.21 mm
Winding turn-to-turn spacing	1 mm
Winding foil thickness	50 μ m
Total notch angle in outer shell	$\pi/3$
Number of notches	4
Core material	Fair-rite 67

Table 5.3: Updated Geometry of the optimized self-shielded inductor post end cap shrinking

5.3 Equivalent Air-core Simulations for Comparison

For a fair comparison, the performance and size of the designed self-shielded cored inductor are compared to two "equivalent" shielded air-core inductor designs. As discussed in Chapter 2, air-core inductors tend to produce fringing flux, leading to EMI concerns. Therefore, these inductors are typically enclosed within a metal shield, which is why shielded air-core inductors serve as an appropriate benchmark for comparison.

Introducing a metal shield around an air-core inductor inevitably leads to a reduction in its inductance. To compensate for this, the shielded air-core inductors are designed with an inherently higher inductance so that, once the shield-induced degradation is accounted for, the resultant inductance matches that of the self-shielded inductor.

To compare the designs based on size and performance, we have set up two distinct

shielded air-core inductors. The first one is designed to match the volume of the self-shielded cored inductor, providing a performance comparison. The air-core inductor has 3 turns, a tube diameter of 7.5 mm, an inner radius of 67 mm, and coil pitch of 16.2 mm. The shield box placed around it is 89 mm tall and has an inner radius of 140 mm. The second one is configured to achieve the same Q as the self-shielded cored inductor, thereby matching the loss and offering a size comparison. The air-core inductor has 4 turns, a tube diameter of 9.5 mm, an inner radius of 58 mm, and coil pitch of 19.53 mm. The shield box placed around it is 75 mm tall and has an inner radius of 80 mm. The results are shown in Table 5.4.

	Self-Shielded Inductor	Shielded Air-Core 1	Shielded Air-Core 2
Volume (L)	1.6	1.6	5.3
Inductance (nH)	470	468	470
Copper Loss (W)	51.54	158	80
Core Loss (W)	33.5	0	0
Total loss (W)	85	158	80
Q	1495	800	1495

Table 5.4: Optimized self-shielded cored inductor compared to equivalent loss and volume shielded air-core inductors

These comparison results offer valuable insights into the superiority of the proposed self-shielded inductor to an air-core inductor. For instance, at a comparable volume, i.e., 1.5L, the self-shielded cored inductor demonstrates a total loss of 86W, a reduction of 45% when compared with the 158W loss of a shielded air-core inductor of the same volume. Furthermore, to achieve a total loss equivalent to the self-shielded cored inductor, the shielded air-core inductor would need to be 3.3x larger in size. This shows that the self-shielded cored inductor offers higher performance within a given volume and presents an opportunity for miniaturization while maintaining an acceptable level of loss.

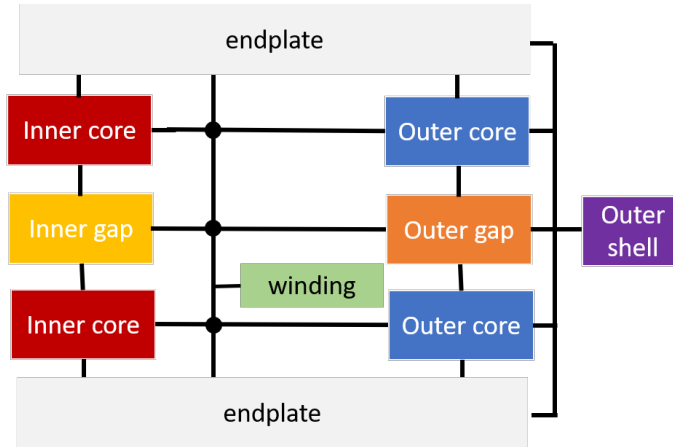


Figure 5-7: Thermal Model in terms of part modules

5.4 Thermal Considerations

While the self-shielded inductor enables us to achieve miniaturization, it simultaneously presents a thermal challenge due to the reduced area available for heat dissipation. Hence, before finalizing our design, one crucial evaluation we must undertake is to assess its thermal viability. To facilitate this, we develop a thermal model to understand the relative impact of change in design parameters. Further, we simulated the design in ANSYS ICEPAK to ensure that the thermal behavior aligns with our expectations and that the system can effectively manage the generated heat under operational conditions.

5.4.1 Thermal Modeling

A 2D thermal model is introduced for the self-shielded inductor based on conductive and convective thermal resistances. The overall system is split into distinct thermal modules as shown in Fig. 5-7. The individual module descriptions are provided in Appendix D. The model is simulated using PLECS, and under an ambient temperature of 22 degrees Celsius, the predicted temperatures for the center post and outer shell are 50°C degrees Celsius and 66°C, respectively.

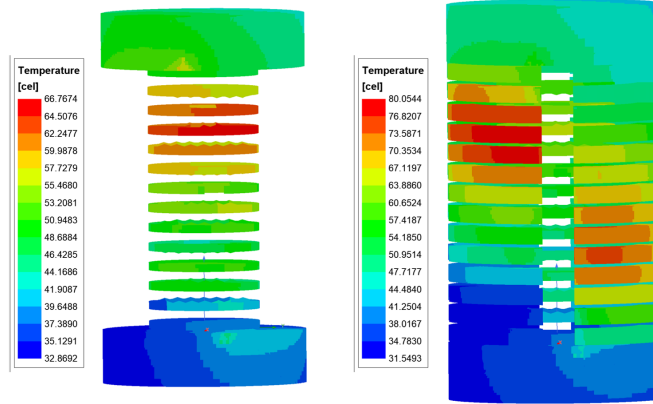


Figure 5-8: ICEPAK simulation of center post, outer shell and end caps @ $T_{\text{ambient}} = 22$ deg Celcius

5.4.2 ICEPAK Simulations

We analyze the thermal heat transfer by conducting an Electrothermal Management (ETM) workflow simulation using Ansys Maxwell and Icepak. Ansys Maxwell allows us to pinpoint the power loss across various sections of the device or system, which serves as the primary source of heat. By integrating these electrical loss profiles into Ansys Icepak, we identify and visualize the heat flow within different parts of the system.

Figure 5-8 illustrates the temperature distribution within the center post, outer shell, and end caps for our proposed inductor when a peak current of 80 Amps is flowing, with an ambient temperature set at 22°C . From the figure, it's noticeable that the maximum temperature in the inner core reaches approximately 67°C . Moreover, the top half of the structure exhibits higher temperatures compared to the lower half due to free convection. Furthermore, the temperature escalates to around 80°C in the outer shell, particularly around the entry and exit points of the input and output terminals. The average center post and outer shell temperature match well with the PLECS model predictions. This thermal performance indicates that our design maintains a safe temperature range under the specified operating conditions.

In applications where the inductor is placed in high-temperature environments, we analyze its thermal robustness at an ambient temperature of 100°C . For these

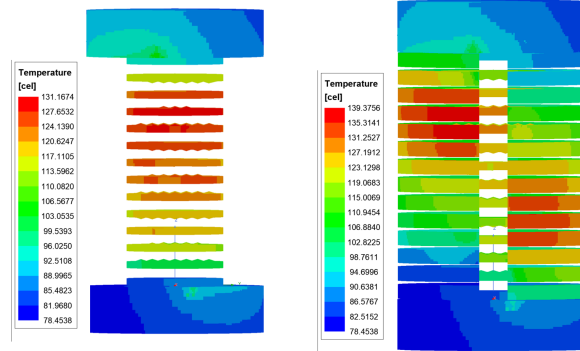


Figure 5-9: ICEPAK simulation of center post, outer shell and end caps @ $T_{\text{ambient}} = 100 \text{ deg Celcius}$

simulations, the ferrite core parameters are adjusted according to the manufacturer's datasheet for operation at 100°C . As shown in Fig. 5-9, the temperature rise (ΔT) is approximately 40°C . The core temperature is well under ferrite's thermal runaway limit and it is safe for operation. The inductor doesn't demand intricate cooling techniques and can be air-cooled.

5.5 Conclusion

The performance of the proposed inductor is verified in simulations and the design proves to be thermally viable and ready for construction and experimental verification!

Chapter 6

Experimental Verification

In this chapter, we cover the construction details of the proposed self-shielded inductor. We also present the details of the Q-measurement setup used to verify the performance of the inductor. Results showcasing the high performance and self-shielded characteristics of the inductor are also shown.

6.1 Construction

We start by selecting material for different parts of our inductor. As mentioned earlier, we use Fair-rite's 67 material due to its superior performance at the frequency of interest [9][3][17]. The core pieces are custom-made orders from fair-rite. The drawings for individual the ferrite parts can be found in Appendix C. To fill in the gaps in the center post and outer shell, we used polypropylene as our non-magnetic spacer material due to its low dielectric loss. Polypropylene sheets of thicknesses 1/4" (for center post) and 3/32" (for outer shell) were ordered from McMaster and machined using a water jet cutter to obtain spacer gap parts for the center post and outer shell as shown in Fig. 6-1. The center post and outer shell individual core pieces are stacked together as shown in Fig. 6-2.

A 50 μ m thick copper foil is selected as our single-layer winding. The copper foil for the desired width (1.181") was obtained from Bridgeport Magnetic Group. The copper foil unlike other winding forms (copper tube) isn't capable of supporting itself



Figure 6-1: Polypropylene non-magnetic spacers cut using a waterjet cutter



Figure 6-2: Center post and one fourth of the outer shell stacked using core pieces and spacer material, number of gaps = 13

and needs to be wrapped on a support structure. This structure is placed between the center post and the copper winding. This structure not only supports the copper foil but also provides insulation between the core pieces and the winding, as well as between the winding turns. The structure also houses the center post core and gap pieces and ensures that they stay concentric. This structure, therefore, needs to be a toroid (in particular, a hollow cylinder). Considering a spacing of 1mm between turns, a dielectric material like Teflon (PTFE, nominally rated for 20kV/mm) can provide sufficient insulation between the turns. PTFE is also characterized by its low dielectric loss, making it an excellent material choice for this structure. One caveat to the use of PTFE in this design is that it cannot be 3D printed and must be machined. Machining a hollow cylinder with a thin wall is a challenging task and can impose constraints on the compactness of the design.

A PTFE hollow cylinder (4" OD x 2-1/2" ID) was obtained from McMaster-CARR and was machined to achieve the desired outer diameter and 2.5 mm wall thickness as shown in Fig. 6-3. The copper foil is wound around the structure using a double-sided tape shown in Fig. 6-4. In order to ensure optimal performance, a 50 μ m thick polyimide tape (PPTDE-1/2) was selected for this purpose. This tape offers excellent

electrical and thermal insulation properties, along with high dielectric strength. In addition, the tape also provides the necessary adhesion to ensure a secure fit for the copper foil. The operating temperature range for this tape is -73 to 260 °C, making it suitable for our operation.



Figure 6-3: PTFE hollow cylinder machined to achieve desired height, outer and inner diameter



Figure 6-4: Cooper foil wrapped around center post through the PTFE support structure using double-sided polyimide tape

Another support structure is required to house the individual outer shell pieces and maintain the notch spacing between them. This structure also is used to support the shield and provide insulation between the copper shield and outer shell core pieces. Although the requirements are similar to the previous structure, using a PTFE-based structure here presents significant machining challenges due to its more complex geometry. We use ULTEM (polyetherimide) for this structure due to its high dielectric strength and excellent physical and thermal properties. ULTEM structures can also be 3D printed, thus allowing to minimize the wall thickness. ULTEM can also handle up to 250 °C before reaching its heat distortion limit. As predicted from our ICEPAK simulations, the inductor temperatures stay well under this limit. So, use of a 3D printed ULTEM structure is thermally feasible.

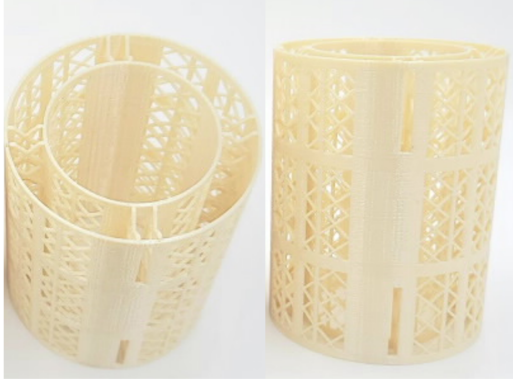


Figure 6-5: 3D printed ULTEM structure to house outer shell and support shield



Figure 6-6: Top view of the center post, outer shell and copper winding

The 3D printed structure (custom printed by 3DGence America) is shown in Fig. 6-5. The structure incorporates a meshed design to allow for air-cooling if required in future design modifications. The inner and outer cylinders have entry and exit slots for winding terminals. The top view of the 3D printed structure housing the outer shell, center post and winding is shown in 6-6.

It can be seen from the loss analysis presented in Chapter 5 that the copper shield contributes less than 10% of the total winding loss. So, a thicker copper foil ($75\mu\text{m}$) is used for shielding as it provides a stable and stiff structure without greatly affecting the inductor performance. In theory, sizing the shield to be $\pi/2$ skin depths would yield a slight reduction in the ac resistance of the shield [13]. Figures 6-7 and 6-8 show the final steps of construction, resulting in a prototype self-shielded inductor thst is ready for testing.

6.2 Experimental setup

The Q-measurement setup used in [3],[17] and briefly discussed in Chapter 2 is considered here. The challenges associated with this setup are discussed and a modified Q-measurement structure is proposed that addresses these challenges.



Figure 6-7: End caps enclosure the center post, winding and outer shell axially



Figure 6-8: $75\mu\text{m}$ thick copper foil is wrapped around the structure to eliminate any fringing fields

6.2.1 Transformer-based Resonant Tank Setup

As shown in Fig. 6-9, the measurement setup in [3],[17] uses the resonant tank technique from [7] to estimate the Q of the inductor. The predominant advantage of this methodology lies in its focus on RF voltage measurements, eliminating the need to grapple with the complexities of RF current measurement. The resistance of the inductor (R_L) as shown in Fig. 6-9. This method estimates the quality factor of the resonant network using the ratio between the voltage across the secondary of the transformer, V_{in} , and the resonant voltage across the vacuum capacitor V_{out} . (R_c) is the equivalent series resistance (ESR) of the vacuum capacitor and can be found in its datasheet. R_x is the additional resistance due to connecting leads of the inductor and can be estimated through FEA simulation.

$$\frac{V_{out}}{V_{in}} = \frac{1}{1 - \omega^2 CL + (j\omega C)(R_L + R_c + R_x)} \quad (6.1)$$

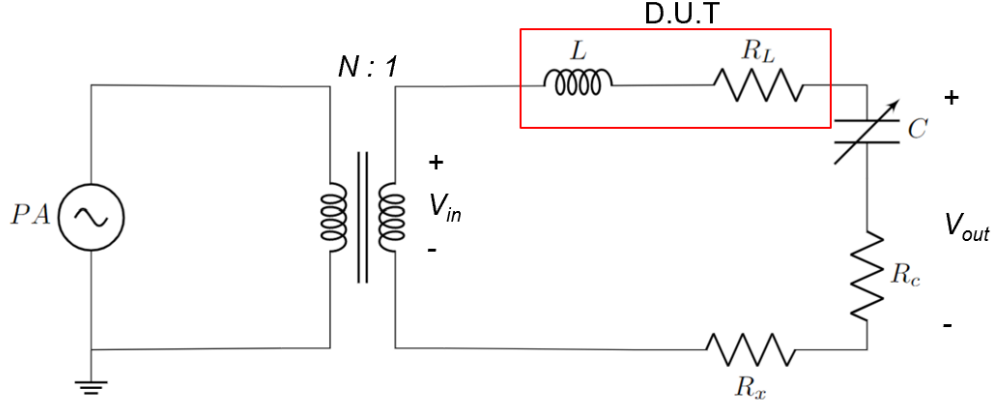


Figure 6-9: Transformer coupled resonant tank experimental setup used in [3],[17] for Q-measurements at high frequency and high current level

At resonance:

$$\frac{V_{out}}{V_{in}} = \frac{1}{\omega C(R_L + R_c + R_x)} \quad (6.2)$$

$$R_L = \omega L \cdot \frac{V_{in}}{V_{out}} - R_x - R_c \quad (6.3)$$

Notably, measuring and characterizing high-power, high-frequency cored inductors is a complex task as the non-linear nature of core loss requires accurate large-signal measurements at the full drive level, $80 A_{pk}$ in our case, which results in several thousand volts across the individual resonant elements. As the resonant tank is connected to the secondary of an N:1 transformer, we can drive our inductor at full drive level without pushing high current through the power amplifier.

The transformer in this setup also helps in impedance matching with the RF amplifier. RF power amplifiers are typically engineered to work with a load impedance of 50Ω . When these power amplifiers are connected to a load with a non- 50Ω impedance, they struggle to transfer power effectively. This impedance mismatch not only diminishes the efficiency of power transfer but also compromises the purity of the signal, introducing distortions and deviating from a perfect sinusoid.

6.2.2 Challenges

The challenges associated with this measurement setup are analyzed and discussed in [17]. A key issue identified was the presence of large common mode currents in the circuit. This was primarily attributed to the breakdown of the isolation barrier, caused by parasitic capacitive coupling between the transformer windings at high frequencies. This issue is further exacerbated by the earth connection present on the oscilloscope, which provides a potential path for current flow. This allows currents to originate from the negative terminal of the power amplifier (which is earthed), then capacitively coupled to the transformer's secondary winding, and finally return to the power amplifier via the oscilloscope's earth connection.

It was found in [17] that Q measurements acquired through conventional voltage probes were not easily reproducible, primarily due to the pervasive common mode noise. A RF detector approach was proposed as a potential solution, converting RF voltages to low-noise DC voltages, with Q estimation based on the DC voltage ratio. However, this method proved less effective than anticipated. Due to the high level of EMI within the system, the multimeter display began to exhibit instability when subjected to higher drive levels (above $10 A_{pk}$).

As the drive level increases, the inductance of the transformer changes. Consequently, the vacuum capacitor requires manual tuning during large signal measurements to ensure we maintain resonance. This is done by looking at the phase shift between the LC tank input voltage (V_{in}) and the capacitor voltage (V_{out}) or when the $|\frac{V_{out}}{V_{in}}|$ ratio is maximum. Hence, it is necessary to have distortion-free and common-mode noise-free waveforms to operate the setup accurately at resonance.

To minimize distortion in our waveforms, we must ensure the power amplifier consistently interfaces with a load close to 50Ω , even at higher drive levels when the resistance of the inductor changes. However, this requirement presents a challenge for this setup. As the transformer's number of turns are fixed, the primary side impedance starts deviating from 50Ω at higher drive levels.

6.2.3 Matching Network and Transformer Resonant Tank Setup

To overcome the challenges mentioned above, we have modified the transformer-based resonant tank setup from [3],[17]. We've introduced a tunable matching network (TMN) between the power amplifier and the transformer as shown in Fig. 6-10. The TMN comprises a shunt variable vacuum capacitor and a series LC branch, which includes an air-core inductor and a variable vacuum capacitor. The capacitance of these variable capacitors can be adjusted, ensuring the impedance viewed by the power amplifier is always close to 50Ω . Additionally, the TMN serves as a low-pass filter, attenuating any higher-order harmonics that may be generated by the power amplifier under unfavorable conditions. MKS Instruments MW2513 model was the TMN used in this case. The air-core inductor is approximately 500 nH and the variable vacuum capacitor go from 50 pF to 500 pF. The capacitance can be controlled by communicating to the TMN through Power Station (MKS software).

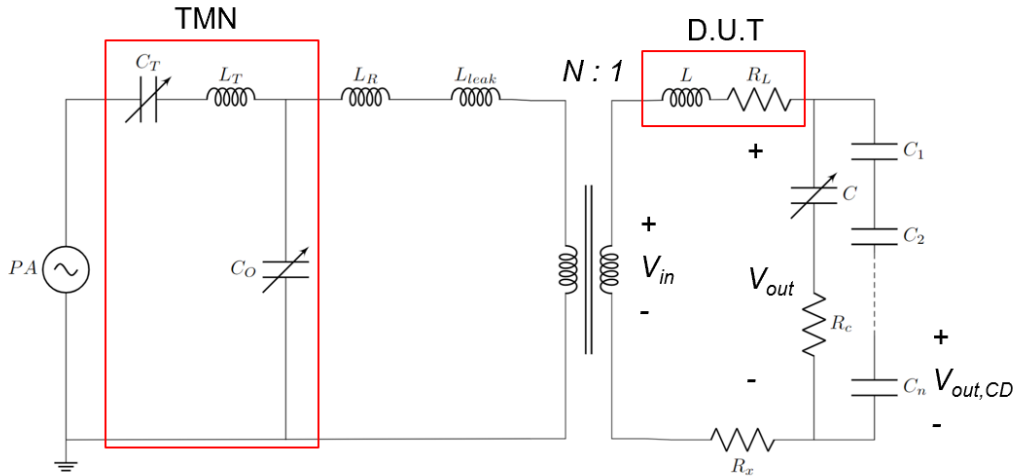


Figure 6-10: Matching network and transformer coupled resonant tank experimental setup for Q-measurements at high frequency and high current level

The current from the power amplifier is now stepped up in two stages; initially, the TMN escalates it by a certain factor, after which the transformer further steps it up to reach higher drive levels (up to $80A_{pk}$) in our inductor. This two-step transformation aids in reducing the number of turns required on the primary side

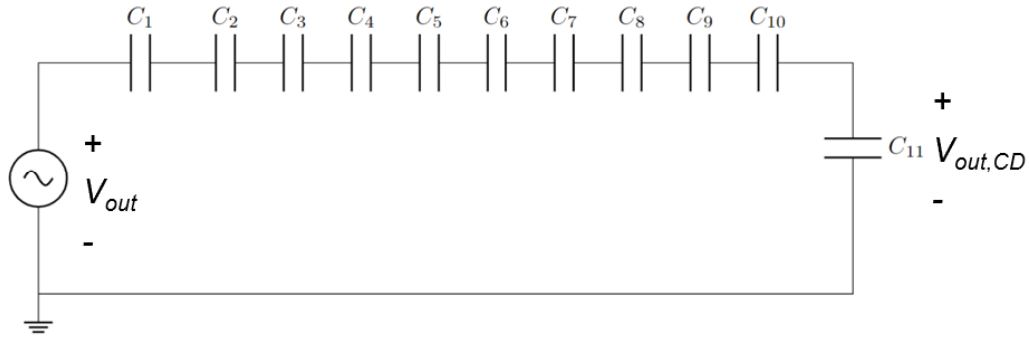


Figure 6-11: Capacitive voltage divider consisting of ten 2.2 pF capacitors in series with a 22 pF capacitor used to measure the resonant voltage across the vacuum capacitor. PCB layout shown Appendix E.

of our transformer. The leakage inductance (L_{leak}) of the transformer is calculated considering its series connection with the shielded inductor. This combination resonates in conjunction with the vacuum capacitor. The transformer was implemented with 7 turns of triple-insulated litz wire (Rubadue wire, 230 strands/44 AWG litz, PN TXXL230/44F3XX-2(MW80)) on a Fair-rite 67 toroid (PN 5967003801). The primary-side leakage inductance of the transformer was found to be $1\mu H$ and the magnetizing inductance was $3\mu H$ through open and short circuit tests. The self-shielded inductor's lead (on the side connected to the vacuum capacitor) serves as the single-turn secondary winding for the transformer. The resistance of these leads (R_x) is estimated to be $7m\Omega$ through FEA simulations.

To minimize the common mode noise present in our measurement waveforms, we utilized optically isolated differential probes, chosen specifically for their high Common Mode Rejection Ratio (CMRR) at our frequency of interest. Tektronix's IsoVu probes (TIVP02) were selected due to their high CMRR at 13.56 MHz [22]. The CMRR of the IsoVu decreases for probe tips with higher differential voltage ranges so to achieve maximum Common mode rejection. Hence, the smallest dynamic voltage range ($\pm 50V$) probe tip (TIVPMX10X) is selected. The MMCX connectors also help with stable test points, high bandwidth, and CMRR.

Due to the high-quality resonance and substantial drive levels, high voltage approximately $5kV$ at the full drive current of $80A_{pk}$, develops across the vacuum ca-

pacitor. Hence, a Comet-PCT 50-500 pF variable vacuum capacitor with a peak RF voltage capability of 9 kV (PN CVPO-500BC/15-BECA) with an ESR ($R_c = 4 \text{ m}\Omega$ at 13.56 MHz) was used to resonate with the D.U.T. To measure this RF voltage through our ($\pm 50\text{V}$) IsoVu probe, we employed a capacitor voltage divider as shown in Fig. 6-11. This consists of a series stack of 10 Mica capacitors, each with a capacitance of 2.2 pF, along with a single 22 pF Mica capacitor (specifically, the Cornell Dubilier Electronics Type MC, in a 1210 size package). This configuration results in an unloaded voltage division ratio of around 1% ie. $V_{out,CD}$ is 1% of the V_{out} . However, it is important to note that in reality, there are parasitic capacitances present in the circuit that can couple to the divided down node across the C_{11} . These parasitic capacitances can have an impact on the actual voltage division ratio of the circuit. It is necessary to consider these parasitic capacitances when analyzing the performance of the voltage divider circuit. the PCB is connected across the vacuum capacitor using copper foil, as illustrated in Fig. 6-12. To calibrate the voltage divider, it is connected in parallel with a 50Ω load. However, during the calibration process, it was discovered that the voltage $V_{out,CD}$ across the divided node connected to the C_{11} capacitor is only 0.3% of the overall output voltage V_{out} . This deviation is primarily caused by the presence of parasitic capacitances within the circuit.

The test environment is depicted in Fig. 6-13. The input voltage of the LC tank (V_{in}) is captured using an IsoVu probe via an MMCX to IC grabber adapter. Another IsoVu probe, connected to the MMCX connector on the voltage divider PCB, measures the voltage ($V_{out,CD}$) across the vacuum capacitor via the capacitive divider.

To maximize the IsoVu probes' common-mode rejection ratio (CMRR), specific measures need to be taken. Firstly, to mitigate capacitive coupling between the IsoVu probes, their heads are positioned to maximize the distance between them. Secondly, the probes should be placed on a tripod to minimize the common-mode parasitic capacitance. Given that the probe heads cannot be bent, the LC tank setup is positioned on a box to bring the test points to the same level.

A coaxial cable is utilized to introduce the required reactance (X_{LR}) to the transformer-coupled LC tank, ensuring it falls within the TMN's matching range.



Figure 6-12: Calibration of the voltage divider ratio to estimate the total voltage across the vacuum capacitor

However, the use of coaxial cable results in the TMN ground and the transformer ground being at different potentials, introducing common mode noise into the system. To address this, the ground of the TMN and the LC tank is shorted using a short copper foil.

6.2.4 Measurement Procedure

- We start by measuring the inductance of our D.U.T at 13.56 MHz using an impedance analyzer (Agilent 4395A). The inductance including the leads was found to be 760 nH and excluding the leads was around 570 nH. we also check the SRF of the design and it was found to be around 50 MHz, close to our design target value of 54 MHz.
- Next, we connect the inductor to the vacuum capacitor and examine the impedance of the LC tank via the transformer's primary side. We then adjust the vacuum capacitor to ensure resonance at 13.56 MHz i.e. $|Z_{min}| @ 13.56 \text{ MHz}$.

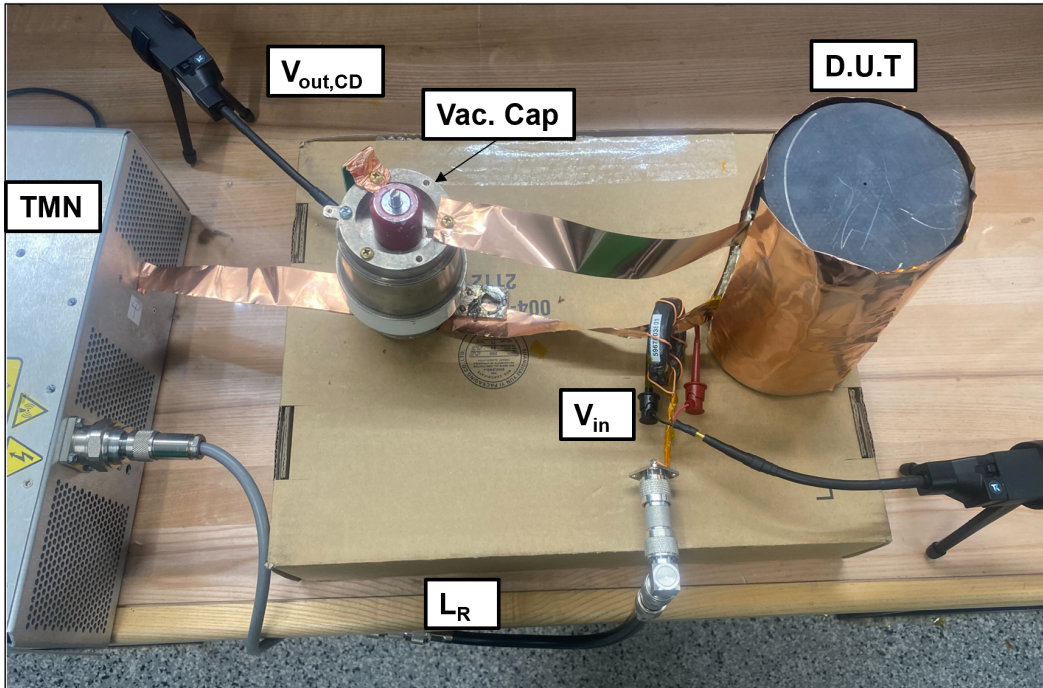


Figure 6-13: An annotated photo of the test setup

- TMN is designed to be able to transform a broad spectrum of impedances to 50Ω . To confirm that we fall within this range, we attempt to estimate the boundaries of this impedance spectrum. It was found that for the TMN to output 50Ω the resistive part needs to be between $2\Omega - 10\Omega$ and the reactive part needs to be between $25\Omega - 70\Omega$.
- We adjust our number of turns on the transformer such that $|Z_{min}|$ is within the TMN's resistive range. As the TMN doesn't work for a purely resistive load, we add some reactance through a long coaxial cable.
- Next, we tune the variable vacuum capacitors in the match to get $50\Omega @ 13.56$ MHz. Set via commands SCO and SCT.
- Connect to the power amplifier and obtain large-signal measurements. An MKS Instruments #000-1106-117 RF V/I probe is placed at the input port to calculate the total input power and the impedance seen by the power amplifier. As the drive level increases, we tune the match to maintain the input impedance as 50Ω .

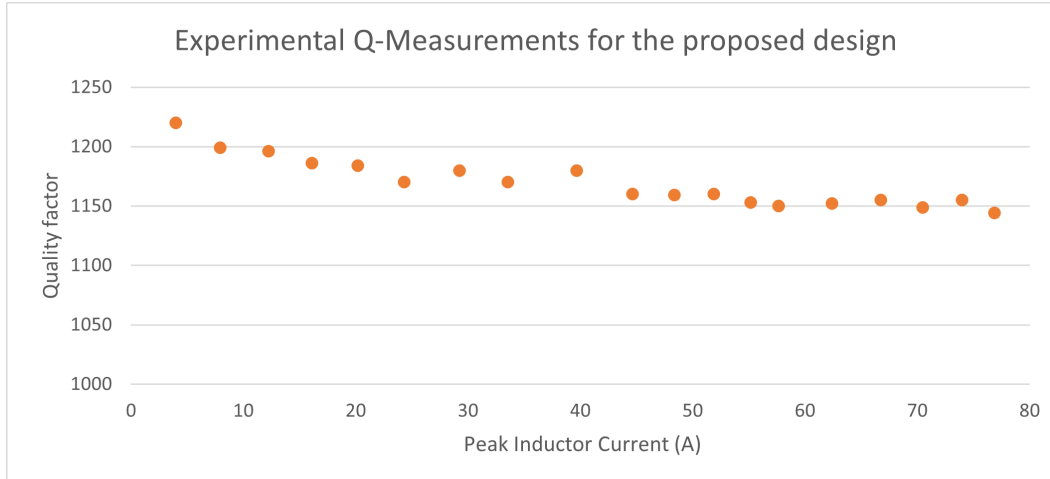


Figure 6-14: Experimental Q-Measurements for the proposed design

6.3 High-Q Results

The performance of the proposed self-shielded inductor is characterized using the measurement setup described above. The inductor is run up to its full drive level i.e. $80A_{pk}$ and the measured-Q values are shown in Fig. 6-14. The results show that the proposed inductor is able to achieve a quality factor of 1150 at its peak current rating. i.e. 80 A at 13.56 MHz. We conducted multiple iterations of the experiment to verify the consistency and repeatability of our result. The self-shielded inductor achieves Q much higher than a similarly sized air-core inductor operating similar conditions. (709 nH, $77.5 A_{pk}$, 10 MHz, $Q = 600$) [1].

The delivered power from the power amplifier is obtained through a power meter and compared to power through our inductor calculated using the voltage measurements. If the delivered power is less than the power through the inductor, it is an indication that the voltage measurements might be contaminated by noise and unreliable. It was found that the power delivered from the power amplifier was greater than that of the inductor, a preliminary indicator that we have minimum noise in the measurement signal¹. Another test was done for the presence of common mode noise in our measured signal, we connected the probe across the same potential. If the probe

¹The Bird power meter and MKS V/I probe were used to measure the delivered power but due to the presence of high EMI, they are unable to operate at higher drive levels (above $55A_{pk}$)

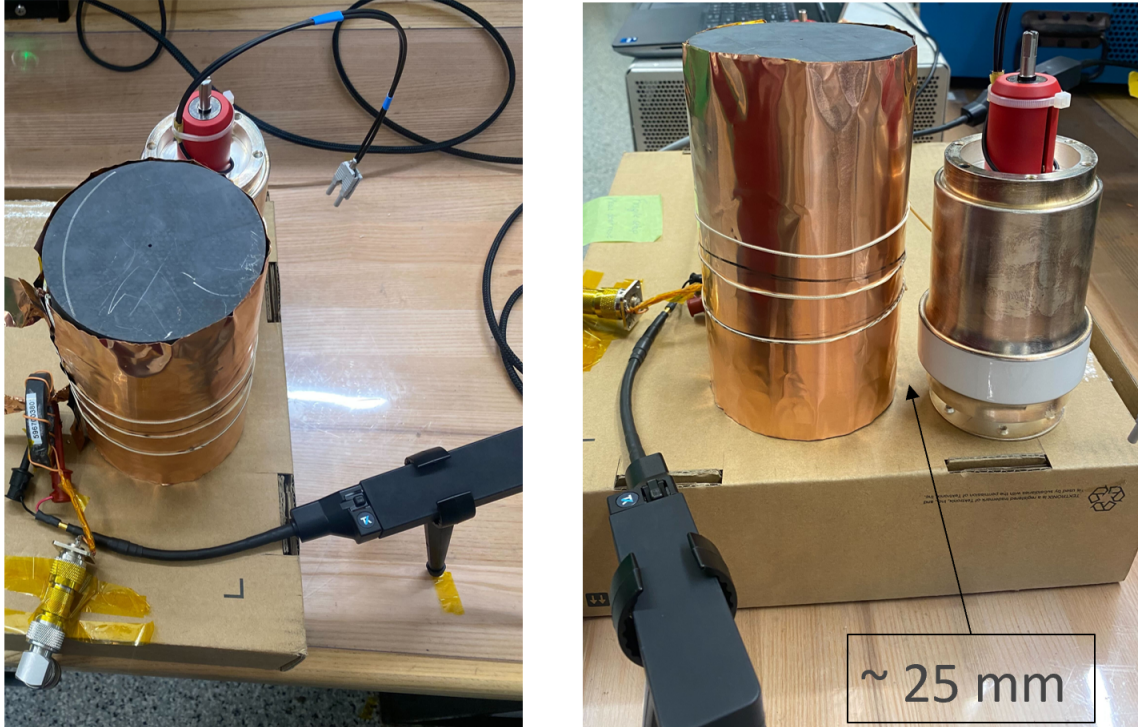


Figure 6-15: Q-measurements of the proposed inductor in close proximity (25 mm) to a vacuum capacitor

picked up any signal in this configuration, it indicates that there is common mode noise present. The common mode noise detected by the IsoVu probes was determined to be less than 10% of the total signal, indicating minimal noise interference.

6.4 Self-Shielding Results

To validate the self-shielding feature of the proposed design, we place a vacuum capacitor close to our inductor in the measurement setup as shown in Fig. 6-15. The Q-measurements are repeated in the presence of the vacuum capacitor and compared to the measurements from the previous case in Fig. 6-16. The data demonstrates that the proximity of the vacuum capacitor to the inductor results in only a 10% reduction in quality factor at the maximum drive level, i.e., at $80A_{pk}$ current. Remarkably, the inductor is still able to attain a high-Q value of 1050, even with a metallic object situated nearby. These results affirm the efficacy of our design's self-shielding

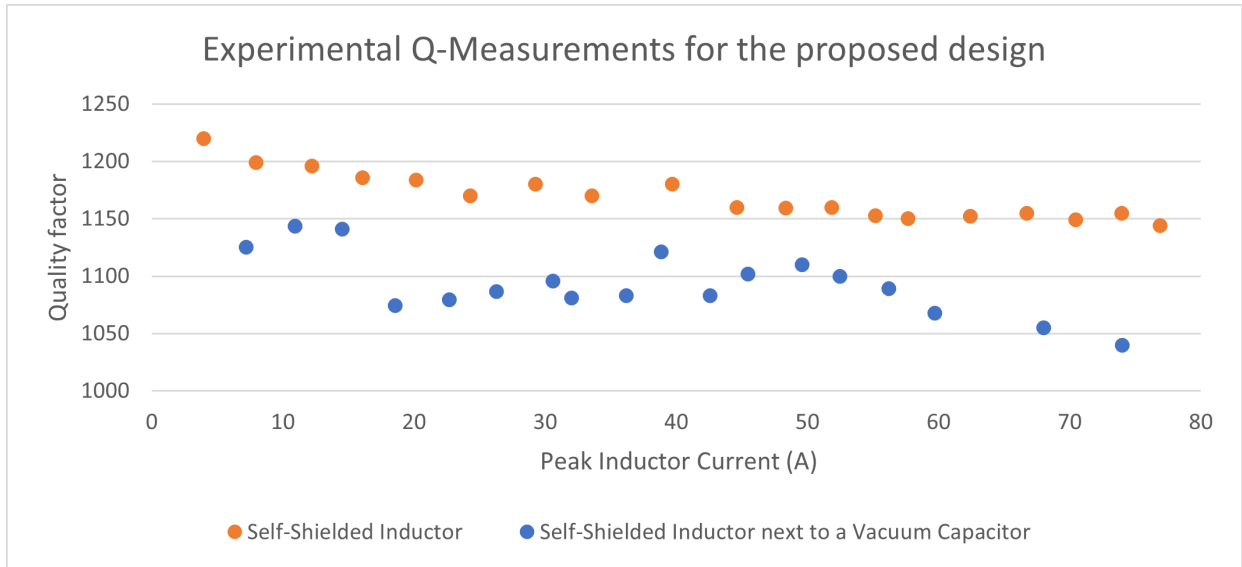


Figure 6-16: Q-measurements to highlight the self-shielded characteristics of the design capabilities, indicating minimal magnetic flux leakage beyond its physical volume.

6.5 Comparison with an Air-Core Inductor

This section presents a comparison of our proposed inductor design with an air-core inductor of similar specifications and also uses air-core measurements to validate the reliability of the measurement setup.

6.5.1 Verification of the Measurement Setup

As a final step to affirm the credibility of the outlined measurement setup, an air-core inductor was designed, with an inductance nearly identical to our proposed inductor. This provides an opportunity to compare the quality factor measured at small signal amplitudes (using an impedance analyzer) to large signal measurements carried out with the matching network and transformer-coupled resonant tank setup.

The inductance of the air-core inductor measured using an impedance analyzer was found to be 585 nH. The air-core inductor is then resonated with a vacuum capacitor to a small-signal measurement for the loss in the inductor at resonance. Since the total impedance of this LC tank will be a couple of m Ω s. However, the



Figure 6-17: Air-core inductor series resonant network with a vacuum capacitor. Air-core specifications : 3 turns of 16 mm copper (wall thickness of 1 mm). Inner radius of the solenoid = 40 mm, pitch = 32 mm.

impedance analyzer used (Agilent 4395A) is not capable of sensing such low values and hence, the 7:1 turn transformer is used to step up the impedance as shown in Fig. 6-17. The minimum impedance of the LC series tank at 13.56 MHz was found to be 67 m Ω . The ESR of the vacuum capacitor (R_c) was 4 m Ω and the resistance of the inductor leads (R_x) was estimated to be 3 m Ω . Thus, the resistance of the air-core inductor (R_L) is estimated to be 60 m Ω and the small-signal Q is 820.

The large-signal measurement is done using the measurement guidelines discussed above. The large-signal Q was found to be approximately 750 for a peak current of 40A_{pk} at 13.56 MHz. The close alignment between the small-signal and large-signal Q measurements (factoring in the EMI losses linked with metal objects in proximity to the test bench) confirms the reliability and accuracy of the measurement setup.

6.5.2 Q-Degradation

Next, a vacuum capacitor is placed next to the air-core inductor as done for the self-shielded inductor in Fig. 6-15, the Q-measurements are repeated and it was observed that the Q drops to 200. This underlines the severe adverse impact of placing metallic objects near air-core inductors, thereby emphasizing the key benefit of self-shielded inductors.

6.6 Conclusion

A compact prototype of a self-shielded inductor with custom support structures and construction guidelines is constructed. An improved measurement setup is developed that uses a tunable matching network and transformer to measure the Q of a high-frequency high-power inductor by resonating it with a variable capacitor. The credibility of the measurement setup is verified through air-core inductor measurements. The high performance of the self-shielded inductor is verified. Furthermore, the experimental results demonstrated that the high performance of the self-shielded inductor remained unaffected even when placed in close proximity to a metal object, providing evidence for the self-shielded nature of the proposed inductor design.

Chapter 7

Conclusion

7.1 Key Takeaways

The design of highly efficient, cored inductors in the high-power RF range is a significant challenge. This thesis builds upon existing techniques for high-frequency cored inductors and presented a design approach and structure for a self-shielded high-power inductor operating at radio frequencies (tens of MHz and hundreds of kW). The accuracy of the design approach and the performance of the proposed structure are verified for example 500 nH self-shielded cored inductor operating at 13.56 MHz with a peak current of 80A. A tunable matching network-based measurement setup is used to measure the performance of the proposed design and to avoid some of the challenges associated with high-frequency high-power measurements. The Q of the proposed structure was verified to be 1150 for a peak current of 80A at 13.56 MHz. This was also compared to a similar specification air-core inductor which had a lower Q of 600.

The performance of the proposed design was also verified in close proximity to other metallic objects, the Q reduced by less than 10% when a vacuum capacitor was placed next to the proposed structure. On repeating the same experiment for an air-core, it was found that the Q drops by more than 50%. The results have validated that the proposed self-shielded high Q inductor can significantly enhance the performance of an RF circuit and reduce its size, leading to higher efficiency and

miniaturization opportunities for high-power RF applications.

7.2 Future Work

Given that the proposed self-shielded design aims to pack more energy in less volume, ensuring thermal viability becomes crucial. As such, it is essential to investigate and address any potential thermal issues that may arise during the operation of the inductor. Since the core pieces are enclosed by the shield, it becomes challenging to directly observe their temperature using a thermal camera. To address this, a potential approach is to employ a fiber optic thermal sensor to measure the temperature of the core pieces. By investigating the thermal aspects of the inductor, any potential overheating issues or limitations can be identified and addressed. This will contribute to the overall characterization and optimization of the inductor's design, enhancing its performance and reliability in high-power RF applications.

The proposed self-shielded inductor structure has the potential to revolutionize RF applications, particularly in the case of tunable matching networks. Currently, air-core inductors are commonly used in these networks, but their size and efficiency limitations pose significant challenges. The performance of a matching network is heavily dependent on the Q of the air-core inductor. The size of the matching network is also dictated by EMI and eddy current losses due to the air-core inductor. By replacing the air-core inductor with the proposed self-shielded inductor structure, significant improvements can be achieved. The high Q value of the self-shielded inductor enhances the efficiency of the matching network, resulting in improved overall performance. Additionally, the compact design of the self-shielded inductor allows for reduced size and miniaturization of the matching network.

To provide a comprehensive comparison and evaluate the efficiency boost offered by the self-shielded inductor, the next step would be to construct a matching network using the self-shielded inductor and compare its efficiency to a matching network utilizing an air-core inductor.

Appendix A

Optimization Script : 2D Model

```
1 clearvars
2 close all
3
4 u_0 = 4*pi*1e-7; % Permeability of free space
5 I = 80; % Peak current excitation
6 f = 13.56e6; % Excitation frequency [Hz]
7 L = 500e-9; % Desired inductance [H]
8 vol = 1e-3; % Desired volume [m^3]
9 rho_cu = 1.8e-8; % Resistivity of copper at 25 C
10 delta = sqrt(rho_cu/(pi*u_0*f)); % Skin depth
11 N_g = 10; % Number of desired gaps
12 l_turn_gap = 1e-3; % Gap b/t adjacent turns
13
14 % FR 67 Parameters
15 u_f = 40; % Relative permeability of ferrite
16 C_m = 1.77925e-6; % P_cv = C_m*f^alpha*B^beta [W/m^3]
17 alpha = 2.202496; % steinmetz freq. param, X in ANSYS
18 beta = 2.118208; % steinmetz b-field param, Y in ANSYS
19
20 P_min = 1e6;
21
22 for N = 1:1:6
23     fprintf("N: %d\r\n", N)
24
```

```

25     for R = 5e-3:1e-3:150e-3
26         for h_e = 5e-3:1e-3:200e-3 % end cap height
27             h_w = vol/(pi*R^2)-2*h_e;
28             cond_area = N*delta/(N+1)*(h_w-(N+2)*l_turn_gap);
29
30             if(h_w < l_turn_gap*(N+2))
31                 continue
32             end
33
34             for b = 0.1:.01:1
35                 for c = 20e-3/R+b:0.01:1
36                     for F_c = 0:N*I
37                         P_cu = rho_cu*pi*R*(b*F_c.^2/cond_area+(I*N-
F_c).^2.*(c/cond_area+1/(delta*h_w)));
38                         R_e = R/(pi*R*h_e*u_f*u_0); % Reluctance of
end cap
39                         R_c = N*F_c/(L*I); % Reluctance of center
post
40                         u_rce = h_w/(R_c*pi*b^2*R^2*u_0); %
Effective relative permeability of center post
41                         f_fc = u_f/(u_rce)*(u_rce-1)/(u_f-1); %
Fraction of ferrite in center post required to achieve u_rce
42                         B_c = L*I/(N*pi*b^2*R^2); % Flux density in
the center post
43                         P_core_c = (f_fc*C_m)*f^alpha*B_c^beta*pi*b
^2*R^2*h_w; % Core loss in center post [W]
44                         R_s = N^2/L-R_c-2*R_e; % Shell reluctance
required to hit F_c, L requirement
45                         u_rse = h_w/(R_s*pi*R^2*(1-c^2)*u_0); %
Effective relative permeability of shell
46                         f_fs = u_f/(u_rse)*(u_rse-1)/(u_f-1); %
Fraction of ferrite in shell required to achieve u_rse
47                         B_s = L*I/(N*pi*R^2*(1-c^2)); % Flux density
in shell
48                         P_core_s = f_fs*C_m*f^alpha*B_s^beta*pi*R
^2*(1-c^2)*h_w; % Core loss in shell [W]

```

```

49         B_end = L*I/(N*pi*R*h_e); % Flux density in
end caps
50         P_core_end = 2*C_m*f^alpha*B_end^beta*pi*R
^2*h_e; % Core loss in end caps
51         P_tot = P_core_s+P_core_c+P_cu+P_core_end;
52
53         if(P_tot<P_min && P_tot>0)
54             P_min = P_tot;
55             P_cu_min = P_cu;
56             P_core_min = P_core_s+P_core_c+
P_core_end;
57             P_core_s_min = P_core_s;
58             P_core_c_min = P_core_c;
59             P_core_end_min = P_core_end;
60             P_shield_min = 1/(2*h_w*delta)*rho_cu*2*
pi*R*(N*I-F_c)^2;
61             b_min = b;
62             c_min = c;
63             F_c_min = F_c;
64             N_min = N;
65             u_rse_min = u_rse;
66             u_rce_min = u_rce;
67             f_fs_min = f_fs;
68             f_fc_min = f_fc;
69             R_min = R;
70             h_e_min = h_e;
71             fprintf("Current P_min: %0.2f [W]\r\n",
P_tot)
72         end
73     end
74 end
75 end
76 end
77 end
78 end
79

```

```

80 Q = 2*pi*f*.5*L*I^2/(P_min);
81
82 h_w_min = vol/(pi*R_min^2)-2*h_e_min;
83 cond_area_min = N_min*delta/(N_min+1)*(h_w_min-(N_min+2)*l_turn_gap)
    ;
84 clc
85
86 fprintf("P_min: %0.3f [W]\r\n",P_min);
87 fprintf("N: %0.1f\r\n",N_min);
88 fprintf("Q: %0.f\r\n",Q)
89 fprintf("Center-post MMF percentage: %0.2f [%%]\r\n",100*F_c_min/(
    N_min*I))
90 fprintf("Outer Radius: %0.2f [mm]\r\n",1e3*R_min)
91 fprintf("End Cap height: %0.2f [mm]\r\n",1e3*h_e_min)
92 fprintf("Center-post radius: %0.2f [mm]\r\n",1e3*b_min*R_min);
93 fprintf('Center disc height: %0.7f [mm]\r\n',1e3*f_fc_min*h_w_min/(
    N_g*(1-f_fc_min)+f_fc_min*(1+N_g)));
94 fprintf("Shell thickness: %0.2f [mm]\r\n",1e3*(1-c_min)*R_min);
95 fprintf('Shell disc height: %0.7f [mm]\r\n',1e3*f_fs_min*h_w_min/(
    N_g*(1-f_fs_min)+f_fs_min*(1+N_g)));
96 fprintf('Center gap pitch: %0.7f [mm]\r\n',1e3*f_fc_min*h_w_min/(N_g
    *(1-f_fc_min)+f_fc_min*(1+N_g))*1/f_fc_min);
97 fprintf('Shell gap pitch: %0.7f [mm]\r\n',1e3*f_fs_min*h_w_min/(N_g
    *(1-f_fs_min)+f_fs_min*(1+N_g))*1/f_fs_min);
98 fprintf('Copper height with 1 mm turn spacing: %0.4f [mm]\r\n', 1e3*
    cond_area_min

```

Appendix B

Optimization Script : 3D Effects Model

```
1 %clear all;
2 close all;
3 clc;
4
5 % To use this script, you must specify: total volume, aspect ratio,
   number
6 % of turns, and the total notch angle. To find the lowest loss
   inductor in
7 % a given volume, another script can be set up which sweeps A and N
   and
8 % plots the lowest total loss.
9
10
11 %% INPUTS:
12 Vtot = 1.5e-3; % total volume [m3]
13 A = 0.45; % aspect ratio, A = 2R/h
14 N = 3; % number of turns
15 L = 500e-9; % desired inductance
16 alpha_notch_deg = 60; % total notch angle
17
18 %% FIXED DESIGN PARAMETERS
```

```

19 I = 80; % peak excitation current (A)
20 f = 13.56e6; %Excitation frequency [Hz]
21
22 %% MATERIAL PARAMETERS
23 mu0 = 4*pi*1e-7; %Permeability of free space
24 mu_f = mu0;
25 rho_cu = 1.8e-8; %Resistivity of copper at 25 C
26 delta = sqrt(rho_cu/(pi*mu0*f)); %Skin depth
27 tw = 50e-6; % thickness of the winding copper
28 tsh = 50e-6; % thickness of the shield copper
29 stt = 1e-3; % spacing between adjacent helix turns
30
31 % FR 67 Parameters
32 mur = 40; %Relative permeability of ferrite
33 C_m = 1.77925e-6; %P_cv = C_m*f^alpha*B^beta [W/m^3]
34 alpha = 2.202496; %steinmetz freq. param, X in ANSYS
35 beta = 2.118208; %steinmetz b-field param, Y in ANSYS
36
37 hc_min = 1e-3;
38 Bmax = 80e-3;
39
40 %% SRF ESTIMATE PARAMETERS
41 eps0 = 8.854*10^-12;
42 c_light = 1/sqrt(eps0*mu0);
43 eps_c = 12; % relative permittivity of the ferrite
44 Z0 = sqrt(mu0/eps0);
45
46 SRF_min = 54;
47 Pmin = inf;
48 k = zeros(5,1);
49
50 %% SEARCH SCRIPT
51 for (N = 2:1:6)
52
53     for (A = 0.1:0.1:0.9)
54 for (Ng=4:2:20)

```



```

55 for(b=0.1:0.05:0.9)
56     for(c=b+0.2:0.05:0.95)
57         for(e=0.05:0.05:0.95)
58             for(ffo=0.05:0.05:0.5)
59                 % find ffi to get inductance
60                 Rtot = (A*Vtot/2/pi)^(1/3); % total radius
61 htot = Vtot/pi/Rtot^2; % total height
62
63                 h_window = e*htot; % window height
64                 he = (htot-h_window)/2; % endcap height
65                 hoc = ffo*h_window/(Ng+1);
66                 hog = (h_window - (Ng+1)*hoc)/Ng;
67                 scsh = hog/4*(Ng/(Ng+1)*ffo + 1);
68                 R = Rtot - scsh-tsh; % radius of the core
69                 hwinding = (h_window-(N+2)*stt)/(N+1); % assume tt
spacing also serves as vertical core-to-helix spacing
70                 alpha_notch = alpha_notch_deg/180*pi;
71
72                 A_ic_z = pi*(b*R)^2;
73                 A_oc_z = pi*(1-c^2)*R^2*(2*pi-alpha_notch)/(2*pi);
74
75                 Rel_oc = hoc/mu0/mur/A_oc_z;
76                 Rel_og = hog/mu0/A_oc_z;
77
78                 gapsLost = 2*(hwinding/(hoc+hog));
79
80                 Ac_phi = R*(1-c)*hoc;
81                 Ac_phi_gap = R*(1-c)*hog;
82                 lc_phi = (2*pi - alpha_notch)*(1+c)/2*R;
83                 Rel_co_phi = lc_phi/(mu0*mur*Ac_phi);
84                 ln_phi = (alpha_notch)*(1+c)/2*R;
85                 Rel_n_phi = ln_phi/(mu0*Ac_phi);
86                 Rel_n_phi_fringe = ln_phi/(mu0*Ac_phi*hog/hoc);
87                 Rel_n_phi = Rel_n_phi*Rel_n_phi_fringe/(Rel_n_phi+
Rel_n_phi_fringe);
88                 l_go_phi = (2*pi)*(1+c)/2*R;

```

```

89         Rel_go_phi = l_go_phi/(mu0*Ac_phi_gap);
90         Rel_net_1 = Rel_co_phi/(Ng+1-gapsLost) + Rel_n_phi/(
Ng+1-gapsLost);
91         Rel_net_2 = Rel_go_phi/(Ng-gapsLost);
92         Rel_net_phi = Rel_net_1*Rel_net_2/(Rel_net_1+
Rel_net_2);
93         Flux_phi_net = I/Rel_net_phi;
94         Flux_phi = I/(Rel_co_phi+Rel_n_phi);
95
96
97         L_phi = 1/Rel_net_phi; %Ng/(Rel_co_phi+Rel_n_phi);
98
99         Rel_endplate = (1+c)/2/pi/he/mur/mu0;
100        Rel_outerpost = Rel_oc*(Ng+1-gapsLost) + Rel_og*(Ng-
gapsLost);
101
102
103        L_z = L-L_phi;
104
105        ffi = 0;
106        for ffiArray=0.01:0.01:0.95
107            hic = ffiArray*h_window/(Ng+1);
108            hig = (h_window - (Ng+1)*hic)/Ng;
109            Rel_ic = hic/mu0/mur/A_ic_z;
110            Rel_ig = hig/mu0/A_ic_z;
111            Rel_centerpost = Rel_ic*(Ng+1-gapsLost) + Rel_ig
*(Ng-gapsLost);
112
113            Rel_crossgap = (c-b)/(c+b)/pi/mu0/hwinding;
114            Rel_lostPath = 0.5*gapsLost*(Rel_oc+Rel_ic+
Rel_og+Rel_ig);
115            Rel_crossgap_net = Rel_crossgap*Rel_lostPath/(
Rel_crossgap+Rel_lostPath);
116
117
118

```

```

119             L_z_temp= N^2/(Rel_centerpost+2*Rel_endplate+
Rel_outerpost+2*Rel_crossgap_net);
120             if (abs(L_z - L_z_temp) < 5e-9)
121                 ffi = ffiArray;
122                 break
123             end
124         end
125
126
127
128         hic = ffi*h_window/(Ng+1);
129         hig = (h_window - (Ng+1)*hic)/Ng;
130         Rel_ic = hic/mu0/mur/A_ic_z;
131         Rel_ig = hig/mu0/A_ic_z;
132         Rel_centerpost = Rel_ic*(Ng+1-gapsLost) + Rel_ig*(Ng
-gapsLost);
133
134         Rel_crossgap = (c-b)/(c+b)/pi/mu0/hwinding;
135         Rel_lostPath = 0.5*gapsLost*(Rel_oc+Rel_ic+Rel_og+
Rel_ig);
136         Rel_crossgap_net = Rel_crossgap*Rel_lostPath/(
Rel_crossgap+Rel_lostPath);
137         fluxRatioUsingCrossGap = Rel_lostPath/(Rel_lostPath+
Rel_crossgap);
138         fluxRatioNotUsingCrossGap = 1-fluxRatioUsingCrossGap
; % this amount of z-flux flows in the lost gaps
139
140
141         L_z = N^2/(Rel_centerpost+2*Rel_endplate+
Rel_outerpost+2*Rel_crossgap_net);
142
143         L_net = L_z + L_phi;
144
145         phi_inner_z = L_z*I/N;
146         phi_inner_z_lostPcs = phi_inner_z*
fluxRatioNotUsingCrossGap;

```

```

147         B_phi = Flux_phi/Ac_phi;
148         B_inner_z = phi_inner_z/A_ic_z;
149         B_outer_z = phi_inner_z/A_oc_z;
150
151         B_inner_z_lostPcs = phi_inner_z_lostPcs/A_ic_z;
152         B_outer_z_lostPcs = phi_inner_z_lostPcs/A_oc_z;
153
154         B_end = phi_inner_z/(pi*R*he);
155         F_c = phi_inner_z*Rel_centerpost +
156         phi_inner_z_lostPcs*gapsLost*(Rel_ic+Rel_ig);
157         F_outer = N*I-F_c - 2*phi_inner_z*Rel_endplate;
158
159         l_winding = 2*pi*(R*(c+b)/2)*N;
160
161         P_inner = 0.5*(rho_cu*l_winding/hwinding/delta)*(F_c
162         ).^2/N^2;
163         P_outer = 0.5*(rho_cu*l_winding/hwinding/delta)*(
164         F_outer).^2/N^2;
165         P_shield = 0.5*(rho_cu*2*pi*Rtot/h_window/delta)*(
166         F_outer).^2;
167
168         B_ci = B_inner_z; % flux density of inner core
169         B_co = sqrt(B_outer_z^2 + B_phi^2); % flux density
170         of outer core
171         Vic = pi*b^2*R^2*hic; % write out the volume of an
172         inner core piece
173         Voc = pi*R^2*(1-c^2)*hoc*(2*pi-alpha_notch)/(2*pi);%
174         write out the volume of an outer core piece
175         Ve = pi*R^2*he;% write out the endcap volume
176
177         P_core_ci = (Ng+1-gapsLost)*C_m*f^alpha*B_ci^beta*
178         Vic+ gapsLost*C_m*f^alpha*B_inner_z_lostPcs^beta*Vic; %Core loss
179         in center post [W]
180         P_core_co = (Ng+1-gapsLost)*C_m*f^alpha*B_co^beta*
181         Voc + gapsLost*C_m*f^alpha*B_outer_z_lostPcs^beta*Voc; %Core loss
182         in outer shell [W]

```

```

172     P_core_e = 2*C_m*f^alpha*B_end^beta*Ve;
173
174     P_core = P_core_ci+P_core_co+P_core_e;
175     Ptot = P_core + P_inner + P_outer + P_shield;
176
177     l = (N+1)*(hwinding)+N*stt;
178     p = hwinding+stt;
179     D = 2*(R*(c+b)/2);
180     psi = atan(p/pi/D);
181     lw = pi*(D)*N/cos(psi); % length of the winding in [
m]
182     %ffi = core height / window height
183     eps_i = ffi*eps_c; % relative permittivity of solid
core coil former
184     eps_x = ffo*eps_c; % relative permeability external
to coil
185     x = pi/2*(D/l) + 0.117*exp(-22*exp(-0.75*l/D)); %
Bessel fn argument
186
187     z_k = 2/pi*l/D;
188     k0 = 1/(log(8/pi)-0.5);
189     k2 = 24/(3*pi^2-16);
190     w = -0.47/(0.755+D/l)^1.44;
191     p0 = k0 + 3.437*l/D + k2*(l/D)^2 + w;
192     kL = z_k*(log(1+1/z_k) + 1/p0); % Nagaoka's
coefficient for use in radial permittivity weighting function
193
194     eps_rad = eps_x/2*(1+kL+eps_i/eps_x*(1-kL)); %
relative permittivity for radial propagation
195
196     I_0_x = besseli(0,x); % modified bessel function of
the first kind, 0th order
197     I_1_x = besseli(1,x); % modified bessel function of
the first kind, 1st order
198
199     K_0_x = bessellk(0,x); % modified bessel function of

```

```

the second kind, 0th order
200         K_1_x = bessellk(1,x); % modified bessel function of
the second kind, 1st order
201
202
203         W_x = sqrt(I_0_x*K_0_x/(I_1_x*K_1_x)); % Ollendorff',
s function
204
205         vhx_div_c = W_x/sqrt(eps_rad); % actual helical
velocity factor
206
207         C_ff_div_D = 2*eps0*eps_rad/(1+log(1+1/D)); % Fringe
field capacitance
208
209         C_af_div_D = eps0*(eps_i+eps_x)/acosh(1.015+(1/D)^2)
; % axial field capacitance
210
211         R0_tan_psi = 1/sqrt(eps_rad)*Z0/(2*pi)*sqrt(2*K_1_x*
I_1_x*K_0_x*I_0_x); % characteristic resistance
212
213         a_SRF = pi/2/vhx_div_c;
214         b_SRF = (1/D)/(c_light*pi*((C_ff_div_D)+(C_af_div_D)
)*(R0_tan_psi));
215
216         diff = 1;
217         n = 1;
218         z = vhx_div_c;
219         while (abs(diff) > 1e-12 && n < 255)
220             y = atan(b_SRF/z)/a_SRF;
221             diff = z-y;
222             der = -(b_SRF/a_SRF)/(z^2+b^2);
223             deltaz = diff/(der-1);
224             z = z+deltaz;
225             n = n+1;
226         end
227         vf_hx_nom = y*c_light;

```

```

228         SRF_MHz = vf_hx_nom/2/lw*1e-6;
229         SRF_MHz_oneEndTiedToInfiniteGndPlane = SRF_MHz/2; %
This is used by Coil64
230         C_ff = C_ff_div_D*D*1e12;
231         C_af = C_af_div_D*D*1e12;
232         psi = atan(p/pi/D);
233         kc = 0.717439*D/l + 0.933048*(D/l)^(3/2) + 0.106*(D/
1)^2;
234         C_Knight = 4*eps0*eps_x/pi*1*(1+kc*(1+eps_i/eps_x)
/2)/(cos(psi))^2*1e12;
235         SRF = SRF_MHz_oneEndTiedToInfiniteGndPlane;
236
237         % Invalidate conditions:
238
239         if (abs(L_z - L_z_temp) > 5e-9)
240             Ptot = inf; % Inductance doesn't match
241         end
242
243
244         if (B_ci > Bmax || B_co > Bmax || B_end > Bmax)
245             Ptot = inf; % flux density too large
246         end
247
248         if (((hig+hic)/4+tw+(hog+hig)/4) > (c-b)*R)
249             Ptot = inf; % doesn't have the right gap spacing
250         end
251
252
253         if (hig < 0 || hoc < 0 || Rel_centerpost < 0)
254             Ptot = inf; % non-physical dimensions
255         end
256
257         if (hic < hc_min || hoc < hc_min)
258             Ptot = inf; % non-physical dimensions
259         end
260

```

```

261         if (SRF < SRF_min)
262             Ptot = inf; % Capacitance too large
263         end
264
265         if (Ptot < 0)
266             Ptot = inf;
267         end
268
269         if (Ptot < Pmin)
270             Pmin = Ptot;
271             b_min = b;
272             c_min = c;
273             e_min = e;
274             ffo_min = ffo;
275             ffi_min = ffi;
276             Ng_min = Ng;
277             N_min = N;
278             A_min = A;
279             alpha_notch_deg_min = alpha_notch_deg;
280         end
281     end
282 end
283 end
284 end
285 end
286 end
287 end
288 end
289 %%
290
291 A = A_min;
292 N = N_min;
293 Ng = Ng_min;
294 b = b_min;
295 c = c_min;
296 e = e_min;

```



```

297 ffo = ffo_min;
298 ffi = ffi_min;
299 alpha_notch_deg = alpha_notch_deg_min;
300
301 display(A);
302 display(N)
303 display(Ng);
304 display(b);
305 display(c);
306 display(e);
307 display(ffo);
308 display(ffi);
309
310 h_window = e*htot; % window height
311 he = (htot-h_window)/2; % endcap height
312 hoc = ffo*h_window/(Ng+1);
313 hic = ffi*h_window/(Ng+1);
314 hog = (h_window - (Ng+1)*hoc)/Ng;
315 hig = (h_window - (Ng+1)*hic)/Ng;
316 scsh = hog/4*(Ng/(Ng+1)*ffo + 1);
317 R = Rtot - scsh-tsh; % radius of the core
318 hwinding = (h_window-(N+2)*stt)/(N+1); % assume tt spacing also
      serves as vertical core-to-helix spacing
319 alpha_notch = alpha_notch_deg/180*pi;
320
321 A_ic_z = pi*(b*R)^2;
322 A_oc_z = pi*(1-c^2)*R^2*(2*pi-alpha_notch)/(2*pi);
323
324 Rel_oc = hoc/mu0/mur/A_oc_z;
325 Rel_og = hog/mu0/A_oc_z;
326
327 gapsLost = 2*(hwinding/(hoc+hog));
328
329 Ac_phi = R*(1-c)*hoc;
330 Ac_phi_gap = R*(1-c)*hog;
331 lc_phi = (2*pi - alpha_notch)*(1+c)/2*R;

```

```

332 Rel_co_phi = lc_phi/(mu0*mur*Ac_phi);
333 ln_phi = (alpha_notch)*(1+c)/2*R;
334 Rel_n_phi = ln_phi/(mu0*Ac_phi);
335 Rel_n_phi_fringe = ln_phi/(mu0*Ac_phi*hog/hoc);
336 Rel_n_phi = Rel_n_phi*Rel_n_phi_fringe/(Rel_n_phi+Rel_n_phi_fringe);
337 l_go_phi = (2*pi)*(1+c)/2*R;
338 Rel_go_phi = l_go_phi/(mu0*Ac_phi_gap);
339 Rel_net_1 = Rel_co_phi/(Ng+1-gapsLost) + Rel_n_phi/(Ng+1-gapsLost);
340 Rel_net_2 = Rel_go_phi/(Ng-gapsLost);
341 Rel_net_phi = Rel_net_1*Rel_net_2/(Rel_net_1+Rel_net_2);
342 Flux_phi_net = I/Rel_net_phi;
343 Flux_phi = I/(Rel_co_phi+Rel_n_phi);
344
345
346 L_phi = 1/Rel_net_phi %Ng/(Rel_co_phi+Rel_n_phi);
347
348 Rel_endplate = (1+c)/2/pi/he/mur/mu0;
349 Rel_outerpost = Rel_oc*(Ng+1-gapsLost) + Rel_og*(Ng-gapsLost);
350
351 Rel_ic = hic/mu0/mur/A_ic_z;
352 Rel_ig = hig/mu0/A_ic_z;
353 Rel_centerpost = Rel_ic*(Ng+1-gapsLost) + Rel_ig*(Ng-gapsLost);
354
355 Rel_crossgap = (c-b)/(c+b)/pi/mu0/hwinding;
356 Rel_lostPath = 0.5*gapsLost*(Rel_oc+Rel_ic+Rel_og+Rel_ig);
357 Rel_crossgap_net = Rel_crossgap*Rel_lostPath/(Rel_crossgap+
    Rel_lostPath);
358 fluxRatioUsingCrossGap = Rel_lostPath/(Rel_lostPath+Rel_crossgap);
359 fluxRatioNotUsingCrossGap = 1-fluxRatioUsingCrossGap; % this amount
    of z-flux flows in the lost gaps
360
361
362 L_z = N^2/(Rel_centerpost+2*Rel_endplate+Rel_outerpost+2*
    Rel_crossgap_net)
363
364 L_net = L_z + L_phi

```

```

365
366 phi_inner_z = L_z*I/N;
367 phi_inner_z_lostPcs = phi_inner_z*fluxRatioNotUsingCrossGap;
368 B_phi = Flux_phi/Ac_phi;
369
370 B_inner_z = phi_inner_z/A_ic_z;
371 B_outer_z = phi_inner_z/A_oc_z;
372
373 B_inner_z_lostPcs = phi_inner_z_lostPcs/A_ic_z;
374 B_outer_z_lostPcs = phi_inner_z_lostPcs/A_oc_z;
375
376 B_end = phi_inner_z/(pi*R*he);
377 F_c = phi_inner_z*Rel_centerpost + phi_inner_z_lostPcs*gapsLost*(
    Rel_ic+Rel_ig);
378 F_outer = N*I-F_c - 2*phi_inner_z*Rel_endplate;
379
380 l_winding = 2*pi*(R*(c+b)/2)*N;
381
382 P_inner = 0.5*(rho_cu*l_winding/hwinding/delta)*(F_c).^2/N^2;
383 P_outer = 0.5*(rho_cu*l_winding/hwinding/delta)*(F_outer).^2/N^2;
384 P_shield = 0.5*(rho_cu*2*pi*Rtot/h_window/delta)*(F_outer).^2;
385
386 B_ci = B_inner_z; % flux density of inner core
387 B_co = sqrt(B_outer_z^2 + B_phi^2); % flux density of outer core
388 Vic = pi*b^2*R^2*hic; % write out the volume of an inner core piece
389 Voc = pi*R^2*(1-c^2)*hoc*(2*pi-alpha_notch)/(2*pi); % write out the
    volume of an outer core piece
390 Ve = pi*R^2*he; % write out the endcap volume
391
392 P_core_ci = (Ng+1-gapsLost)*C_m*f^alpha*B_ci^beta*Vic + gapsLost*C_m*
    f^alpha*B_inner_z_lostPcs^beta*Vic; %Core loss in center post [W]
393 P_core_co = (Ng+1-gapsLost)*C_m*f^alpha*B_co^beta*Voc + gapsLost*C_m
    *f^alpha*B_outer_z_lostPcs^beta*Voc; %Core loss in outer shell [W
    ]
394 P_core_e = 2*C_m*f^alpha*B_end^beta*Ve;
395

```

```

396 P_core = P_core_ci+P_core_co+P_core_e;
397 Ptot = P_core + P_inner + P_outer + P_shield;
398
399 l = (N+1)*(hwinding)+N*stt;
400 p = hwinding+stt;
401 D = 2*(R*(c+b)/2);
402 psi = atan(p/pi/D);
403 lw = pi*(D)*N/cos(psi); % length of the winding in [m]
404 %ffi = core height / window height
405 eps_i = ffi*eps_c; % relative permittivity of solid core coil former
406 eps_x = ffo*eps_c; % relative permeability external to coil
407 x = pi/2*(D/l) + 0.117*exp(-22*exp(-0.75*l/D)); % Bessel fn argument
408
409 z_k = 2/pi*l/D;
410 k0 = 1/(log(8/pi)-0.5);
411 k2 = 24/(3*pi^2-16);
412 w = -0.47/(0.755+D/l)^1.44;
413 p0 = k0 + 3.437*l/D + k2*(l/D)^2 + w;
414 kL = z_k*(log(1+1/z_k) + 1/p0); % Nagaoka's coefficient for use in
    radial permittivity weighting function
415
416 eps_rad = eps_x/2*(1+kL+eps_i/eps_x*(1-kL)); % relative
    permittivity for radial propagation
417
418 I_0_x = besseli(0,x); % modified bessel function of the first kind,
    0th order
419 I_1_x = besseli(1,x); % modified bessel function of the first kind,
    1st order
420
421 K_0_x = bess elk(0,x); % modified bessel function of the second kind,
    0th order
422 K_1_x = bess elk(1,x); % modified bessel function of the second kind,
    1st order
423
424
425 W_x = sqrt(I_0_x*K_0_x/(I_1_x*K_1_x)); % Ollendorff's function

```

```

426
427 vhx_div_c = W_x/sqrt(eps_rad); % actual helical velocity factor
428
429 C_ff_div_D = 2*eps0*eps_rad/(1+log(1+1/D)); % Fringe field
      capacitance
430
431 C_af_div_D = eps0*(eps_i+eps_x)/acosh(1.015+(1/D)^2); % axial field
      capacitance
432
433 RO_tan_psi = 1/sqrt(eps_rad)*ZO/(2*pi)*sqrt(2*K_1_x*I_1_x*K_0_x*
      I_0_x); % characteristic resistance
434
435 a_SRF = pi/2/vhx_div_c;
436 b_SRF = (1/D)/(c_light*pi*((C_ff_div_D)+(C_af_div_D))*(RO_tan_psi));
437
438 diff = 1;
439 n = 1;
440 z = vhx_div_c;
441 while (abs(diff) > 1e-12 && n < 255)
442     y = atan(b_SRF/z)/a_SRF;
443     diff = z-y;
444     der = -(b_SRF/a_SRF)/(z^2+b^2);
445     deltaz = diff/(der-1);
446     z = z+deltaz;
447     n = n+1;
448 end
449 vf_hx_nom = y*c_light;
450 SRF_MHz = vf_hx_nom/2/lw*1e-6;
451 SRF_MHz_oneEndTiedToInfiniteGndPlane = SRF_MHz/2; % This is used by
      Coil64
452 C_ff = C_ff_div_D*D*1e12;
453 C_af = C_af_div_D*D*1e12;
454 psi = atan(p/pi/D);
455 kc = 0.717439*D/l + 0.933048*(D/l)^(3/2) + 0.106*(D/l)^2;
456 C_Knight = 4*eps0*eps_x/pi*1*(1+kc*(1+eps_i/eps_x)/2)/(cos(psi))^2*1
      e12;

```

```

457 SRF = SRF_MHz_oneEndTiedToInfiniteGndPlane;
458
459
460 P_oc = P_core_co;
461 P_ic = P_core_ci;
462 P_w = P_inner + P_outer;
463 P_s = P_shield;
464 P_e = P_core_e;
465
466
467 Pcu = P_w+P_s;
468 display(Pcu);
469 display(P_core);
470 display(Ptot);
471 display(C_Knight);
472 display(SRF);
473 display(B_inner_z);
474 display(B_outer_z);
475 display(B_phi)
476
477 display(F_c);
478 display(F_outer);
479
480 display(P_oc);
481 display(P_ic);
482 display(P_w);
483 display(P_s);
484
485 display(P_e);
486
487 hic_mm = hic*1e3
488 hig_mm = hig*1e3
489 hoc_mm = hoc*1e3
490 hog_mm = hog*1e3
491
492 Rtot_mm = Rtot*1e3

```

```
493 R_mm = R*1e3
494 innerRad = b*R*1e3
495 outerRad = c*R*1e3
496 scsh_mm = scsh*1e3
497
498 helixRad = (b+c)*R/2*1e3
499 hwinding_mm=hwinding*1e3
500 he_mm = he*1e3
```

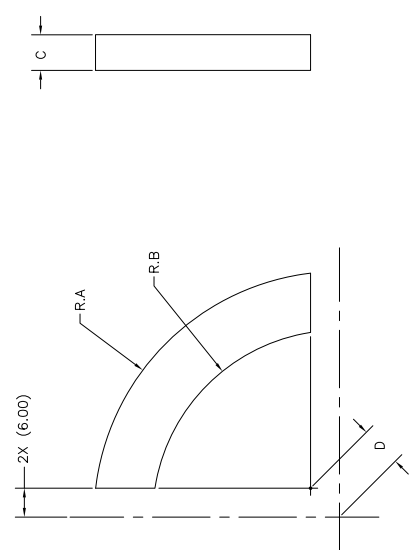

Appendix C

Ferrite core Drawings

UNCONTROLLED COPY WHEN PRINTED		SIZE	PART NO.	REV.
		B	8367000746	0

NOTES:

- 1 - MACHINE FROM APPROVED FR# 67 MATERIAL BLOCK.
- 2 - MILLIMETERS ARE THE CONTROLLING UNITS OF MEASURE.
- 3 - ALL DIMENSIONS, TOLERANCES, GEOMETRIC DIMENSIONING AND TOLERANCING, SURFACE FINISHES, AND NOTES SHALL BE AS SHOWN.
- 4 - FAIR-RITE STANDARD METHODS AND SPECIFICATIONS SHALL APPLY. ANY NOTES, STANDARD TOLERANCES, STANDARD SURFACE FINISHES, ETC. ON THE CUSTOMER PRINT NOT SHOWN ON THIS DRAWING, OR IN FAIR-RITE'S STANDARD DOCUMENTATION, SHALL NOT APPLY.



REV.	ECN	DESCRIPTION	DRFT	DATE

APPLICABLE SPECS	DRAWING CLASS	MATERIAL	TITLE	REV.
		FR# 67	FAIR-RITE PRODUCTS CORP.	
Tolerances Unless Otherwise Indicated	FINISH	MACHINED OUTER CORE	DRAWN BY	SIZE PART NO.
2PL			J-CUSTY	B 8367000746
3PL			CHKD BY	
FRACT			APPRVD BY	
ANGLE				SCALE NONE
				SHEET 1 of 1

A (KEY)	B (KEY)	C (1M)	D (KEY)
50.873 / 51.127	38.693 / 38.947	7.273 / 7.527	8.359 / 8.613
2.0079 ± .0050	1.5283 ± .0050	.2913 ± .0050	.3341 ± .0050

BOLD DIMENSIONS ARE IN MILLIMETERS,** LIGHT NUMBERS ARE IN INCHES

ADDED TO SYSTEM PER ECN# D-####

Figure C-2: Drawing of Ferrite outer shell Piece

Appendix D

Thermal Model

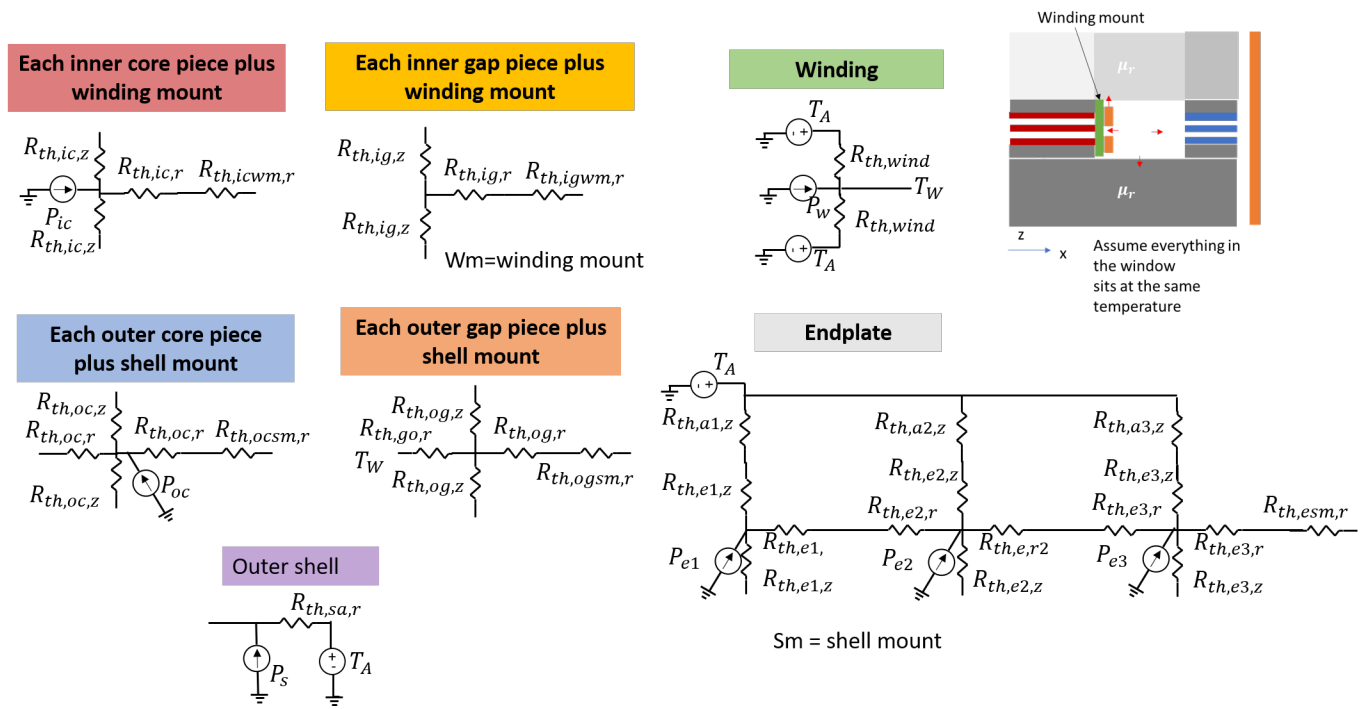


Figure D-1: Thermal resistance 'modules' used to define thermal resistance network

	Parameter	Equation	Description
Inner core piece plus winding mount	$R_{th,ic,z}$	$\rho_{ferrite} \frac{h_{ic}}{2} \pi (bR)^2$	From center of an inner core piece to the top or bottom h_{ci} is the inner core piece height
	$R_{th,ic,r}$	$\rho_{ferrite} \frac{1}{\pi h_{ic}}$	“Radial” thermal resistance from center to window Take average cross-sectional area as $\pi h_{ci}(bR)$. (mean of circumference*h from 0 to bR). Length is bR
	$R_{th,icwm,r}$	$\rho_{spacer,w} \frac{s_{ct}}{\pi h_{ic}(s_{ct} + 2bR)}$	“Radial” thermal resistance of winding mount Take average cross-sectional area as $\frac{2\pi h_{ci}(s_{ct}+bR+bR)}{2}$ Length is s_{ct} Assumes that the heat will convect in the small part of the spacer that it attaches to
Each inner gap piece plus winding mount	$R_{th,ig,z}$	Same as $R_{th,ic,z}$ but with h_{ig} and ρ_{gap}	Z-Rth to the middle of the gap h_{gi} is the inner core piece height
	$R_{th,ig,r}$	Same as $R_{th,ic,r}$ but with h_{ig} and ρ_{gap}	r-Rth from the center to the window
	$R_{th,igwm,r}$	Same as $R_{th,icwm,r}$ but with h_{ig}	r-Rth from the edge of the window to the winding
Inner Support Pieces	$R_{th,is,z}$	Same as $R_{th,ic,z}$ but with h_f	z-Rth to the middle of the inner support piece
	$R_{th,is,r}$	Same as $R_{th,ic,r}$ but with h_f	r-Rth to the core window from the middle of the inner support piece
	$R_{th,ism,r}$	Same as $R_{th,icwm,r}$ but with h_f	r-Rth of the holder of the copper winding
Each outer core piece plus shell mount	$R_{th,oc,z}$	Same as $R_{th,ic,z}$ but with h_{ic} changed to h_{oc} $(bR)^2 \rightarrow (1 - c^2)R^2$	
	$R_{th,oc,r}$	$\rho_{ferrite} \frac{(1 - c)}{2\pi h_{oc}(1 + c)}$	“Radial” thermal resistance from center of outer shell. Take average cross-sectional area as $\pi h_{co}(R(1 + c))$. (mean of circumference*h from cR to R). Length is $(R-cR)/2 = (1-c)R/2$
	$R_{th,ocsm,r}$	$\rho_{spacer,s} \frac{s_{ct}}{\pi h_{oc}(s_{ct} + 2R)}$	$\rho_{spacer,s}$ is the spacer used to mount the shell. Take average cross-sectional area as $\frac{2\pi h_{ci}(s_{ct}+R+R)}{2}$

Figure D-2: First set of thermal resistances used in the thermal model.

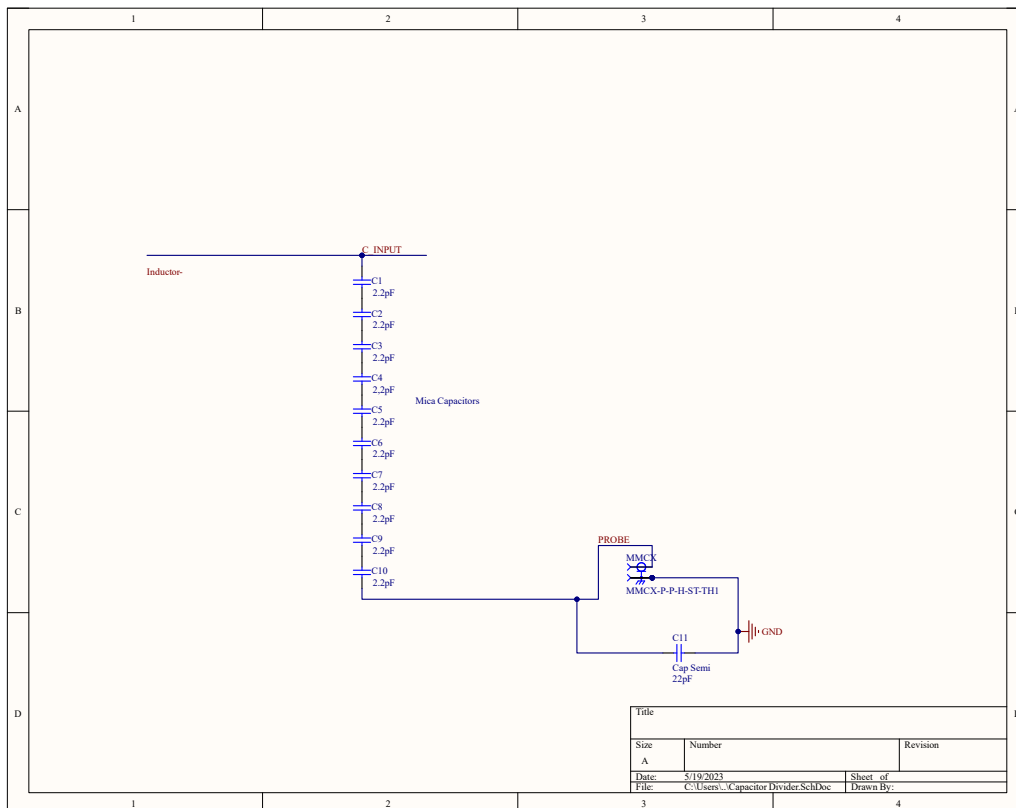
	Parameter	Equation	Description
Each outer gap piece plus shell mount	$R_{th,og,z}$	Same as $R_{th,oc,z}$ but with h_{og} and ρ_{gap}	
	$R_{th,og,r}$	Same as $R_{th,oc,r}$ but with h_{og} and ρ_{gap}	
	$R_{th,ogsm,r}$	Same as $R_{th,ocsm,r}$ but with h_{og}	
Endplate	$R_{th,ea1,z}$	$h_{air} \pi (bR)^2$	Forced air convective cooling $h_{air} = 12.12 - 1.16 v + 11.6 v$
	$R_{th,e1,z}$	$R_{th,ic,z}$, change $h_{ic} \rightarrow h_e$	To the middle of the endplate in the z direction
	$R_{th,e1,r}$	$R_{th,ic,r}$, change $h_{ic} \rightarrow h_e$	To the edge of the endplate portion in the r direction
	$R_{th,ea2,z}$	$h_{air} \pi R^2 (c^2 - b^2)$	To the middle of the endplate in the second portion
	$R_{th,e2,z}$	Same as $R_{th,ic,z}$ but with $h_{ic} \rightarrow h_e$ $(bR)^2 \rightarrow (c^2 - b^2)R^2$	
	$R_{th,e2,r}$	$\rho_{ferrite} \frac{(c-b)}{2\pi h_e (c+b)}$	
	$R_{th,ea3,z}$	$h_{air} \pi R^2 (1 - c^2)$	
	$R_{th,e3,z}$	Same as $R_{th,oc,z}$ but with $h_{oc} \rightarrow h_e$	
	$R_{th,e3,r}$	$R_{th,oc,r}$ $h_{oc} \rightarrow h_e$	
		$R_{th,esm,r}$	$R_{th,ocsm,r}$ $h_{oc} \rightarrow h_e$
Outer shell	$R_{th,sa,r}$	$h_{air} (2\pi R)(2h_e + h_w)$	
Winding	$R_{th,wind}$	370 W/m.K	
		$\frac{l_{winding}}{A_{winding}}$	

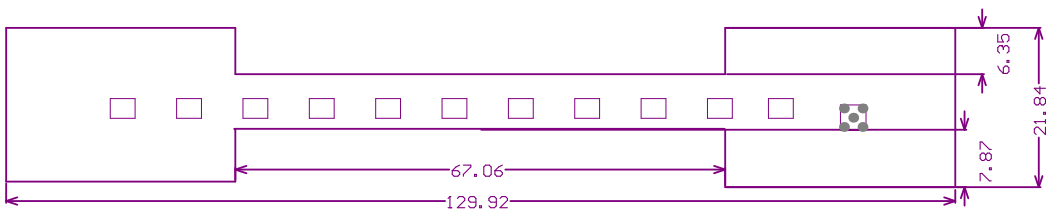
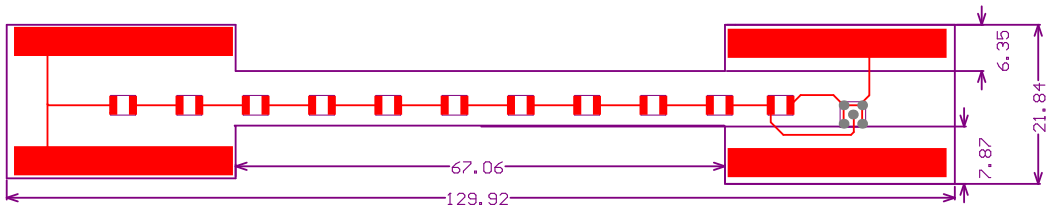
Figure D-3: Second set of thermal resistances used in the thermal model.

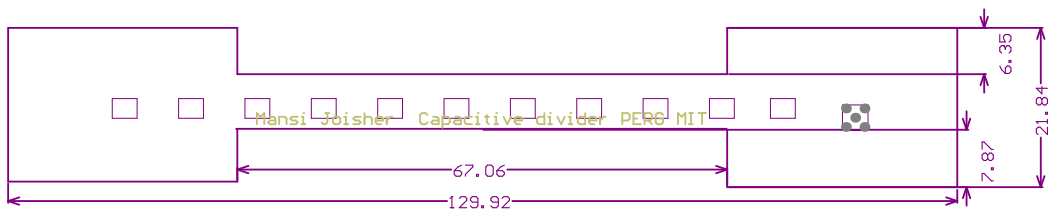
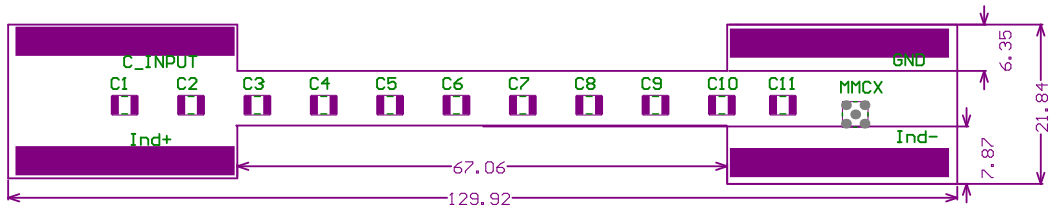
Appendix E

Voltage Divider PCB

Capacitive voltage divider PCB and Schematic. Mechanical design dimensions shown in mm.







Bibliography

- [1] Anas Al Bastami, Alexander Jurkov, David Otten, Duy T. Nguyen, Aaron Radomski, and David J. Perreault. A 1.5 kw radio-frequency tunable matching network based on phase-switched impedance modulation. *IEEE Open Journal of Power Electronics*, 1:124–138, 2020.
- [2] Mike Ranjram Author. Refining the shielded inductor, 2021. Internal document.
- [3] Roderick S. Bayliss, Rachel S. Yang, Alex J. Hanson, Charles R. Sullivan, and David J. Perreault. Design, implementation, and evaluation of high-efficiency high-power radio-frequency inductors. In *2021 IEEE Applied Power Electronics Conference and Exposition (APEC)*, pages 881–888, 2021.
- [4] Fairrite. Low loss 67 material for high frequency power applications. <https://www.fair-rite.com/wp-content/uploads/2016/04/Low-Loss-67-Material-for-High-Frequency-Power-Applications-for-website.pdf>.
- [5] Ferroxcube. Soft ferrites. http://ferroxcube.home.pl/prod/assets/sfmatgra_frnt.pdf.
- [6] E. I. Green. The story of q. *American Scientist*, 43:584–594, Oct. 1955.
- [7] Yehui Han, Grace Cheung, An Li, Charles R. Sullivan, and David J. Perreault. Evaluation of magnetic materials for very high frequency power applications. *IEEE Transactions on Power Electronics*, 27(1):425–435, 2012.
- [8] Yehui Han and David J. Perreault. Inductor design methods with low-permeability rf core materials. *IEEE Transactions on Industry Applications*, 48(5):1616–1627, 2012.
- [9] Alex J. Hanson, Julia A. Belk, Seungbum Lim, Charles R. Sullivan, and David J. Perreault. Measurements and performance factor comparisons of magnetic materials at high frequency. *IEEE Transactions on Power Electronics*, 31(11):7909–7925, 2016.
- [10] Jiankun Hu and C.R. Sullivan. The quasi-distributed gap technique for planar inductors: design guidelines. In *IAS '97. Conference Record of the 1997 IEEE Industry Applications Conference Thirty-Second IAS Annual Meeting*, volume 2, pages 1147–1152 vol.2, 1997.

- [11] J.G. Kassakian, D.J. Perreault, G.C. Verghese, and M.F. Schlecht. *Chapter 19*. Cambridge University Press, 2nd edition, 2023.
- [12] J.G. Kassakian, D.J. Perreault, G.C. Verghese, and M.F. Schlecht. *Chapter 20*. Cambridge University Press, 2nd edition, 2023.
- [13] J.G. Kassakian, D.J. Perreault, G.C. Verghese, and M.F. Schlecht. *Chapter 20*. Cambridge University Press, 2nd edition, 2023.
- [14] David W. Knight. The self-resonance and self-capacitance of solenoid coils: applicable theory, models and calculation methods.
- [15] E. R. Laithewaite. Magnetic equivalent circuits for electrical machines. *Proceedings of the Institution of Electrical Engineers*, 114(11):1805–1809, November 1967.
- [16] David J. Perreault, Jingying Hu, Juan M. Rivas, Yehui Han, Olivia Leitermann, Robert C.N. Pilawa-Podgurski, Anthony Sagneri, and Charles R. Sullivan. Opportunities and challenges in very high frequency power conversion. In *2009 Twenty-Fourth Annual IEEE Applied Power Electronics Conference and Exposition*, pages 1–14, 2009.
- [17] Roderick S. Bayliss III. Design, implementation, and evaluation of high-efficiency high-power radio-frequency inductors. Master of engineering in electrical engineering and computer science, Massachusetts Institute of Technology, 2021.
- [18] T.L. Simpson. Effect of a conducting shield on the inductance of an air-core solenoid. *IEEE Transactions on Magnetics*, 35(1):508–515, 1999.
- [19] Michael Solomentsev and Alex J. Hanson. At what frequencies should air-core magnetics be used? *IEEE Transactions on Power Electronics*, 38(3):3546–3558, 2023.
- [20] Charles Proteus Steinmetz. On the law of hysteresis. *Proceedings of the IEEE*, 72:197–221, 1984.
- [21] Charles R. Sullivan. Prospects for advances in power magnetics. In *CIPS 2016; 9th International Conference on Integrated Power Electronics Systems*, pages 1–9, 2016.
- [22] Tektronix. Isolated measurement systems. <https://www.tek.com/en/datasheet/isolated-measurement-systems-tivp1-tivp05-tivp02-datasheet>.
- [23] Rachel S. Yang, Alex J. Hanson, Bradley A. Reese, Charles R. Sullivan, and David J. Perreault. A low-loss inductor structure and design guidelines for high-frequency applications. *IEEE Transactions on Power Electronics*, 34(10):9993–10005, 2019.

- [24] Rachel S. Yang, Alex J. Hanson, Charles R. Sullivan, and David J. Perreault. Design flexibility of a modular low-loss high-frequency inductor structure. *IEEE Transactions on Power Electronics*, 36(11):13013–13024, 2021.
- [25] Grayson Zulauf and Juan M. Rivas-Davila. Single-turn air-core coils for high-frequency inductive wireless power transfer. *IEEE Transactions on Power Electronics*, 35(3):2917–2932, 2020.